Article

Developmental Cell

Direct Microtubule-Binding by Myosin-10 Orients Centrosomes toward Retraction Fibers and Subcortical Actin Clouds

Highlights

- Myo10 orients centrosomes toward retraction fibers and subcortical actin clouds
- Spindle positioning by Myo10 requires its direct microtubule binding
- Myo10 and cortical dynein have distinct effects on cortical-microtubule interactions
- Myo10 and cortical dynein overlap to promote spindle positioning in mammalian cells

Authors

Mijung Kwon, Maria Bagonis, Gaudenz Danuser, David Pellman

Correspondence

mijung_kwon@dfci.harvard.edu (M.K.), david_pellman@dfci.harvard.edu (D.P.)

In Brief

In mammalian cells, the mitotic spindle is oriented toward extracellular cues via retraction fibers and associated subcortical actin clouds. Kwon et al. shed light on how actin influences spindle positioning and show that the unconventional microtubule-binding myosin Myo10 couples these actin-dependent forces to microtubule dynamics, microtubule-cortical interactions, and spindle positioning.

Kwon et al., 2015, Developmental Cell *34*, 323–337
August 10, 2015
http://dx.doi.org/10.1016/j.devcel.2015.06.013

CellPress

Developmental Cell
Article

Direct Microtubule-Binding by Myosin-10 Orients Centrosomes toward Retraction Fibers and Subcortical Actin Clouds

Mijung Kwon,[1,2,*] Maria Bagonis,[2] Gaudenz Danuser,[2] and David Pellman[1,2,*]
[1]Department of Pediatric Oncology, Howard Hughes Medical Institute, Dana-Farber Cancer Institute, Boston, MA 02215, USA
[2]Department of Cell Biology, Harvard Medical School, Boston, MA 02115, USA
*Correspondence: mijung_kwon@dfci.harvard.edu (M.K.), david_pellman@dfci.harvard.edu (D.P.)
http://dx.doi.org/10.1016/j.devcel.2015.06.013

SUMMARY

Positioning of centrosomes is vital for cell division and development. In metazoan cells, spindle positioning is controlled by a dynamic pool of subcortical actin that organizes in response to the position of retraction fibers. These actin "clouds" are proposed to generate pulling forces on centrosomes and mediate spindle orientation. However, the motors that pull astral microtubules toward these actin structures are not known. Here, we report that the unconventional myosin, Myo10, couples actin-dependent forces from retraction fibers and subcortical actin clouds to centrosomes. Myo10-mediated centrosome positioning requires its direct microtubule binding. Computational image analysis of large microtubule populations reveals a direct effect of Myo10 on microtubule dynamics and microtubule-cortex interactions. Myo10's role in centrosome positioning is distinct from, but overlaps with, that of dynein. Thus, Myo10 plays a key role in integrating the actin and microtubule cytoskeletons to position centrosomes and mitotic spindles.

INTRODUCTION

The regulated positioning of centrosomes within cells has essential roles in tissue homeostasis, morphogenesis, and the specification of cell fate during development (McNally, 2013; Morin and Bellaïche, 2011). In symmetrically dividing cells, centrosome positioning centers the mitotic spindle, which is important for maintaining normal daughter cell size (Kiyomitsu and Cheeseman, 2013). Centrosome and spindle positioning is also important for asymmetric cell divisions, which control some cell fate decisions during development and are required for stem cell maintenance (McCaffrey and Macara, 2011; Morin and Bellaïche, 2011; Siller and Doe, 2009). Defects in spindle positioning are implicated in developmental defects and tumorigenesis (McCaffrey and Macara, 2011; Pease and Tirnauer, 2011).

Centrosome positioning is controlled by mechanisms that differ between cell types. In the simplest case, pushing forces from polymerizing microtubules can center asters in cell fragments (Rodionov and Borisy, 1998) and microfabricated chambers (Laan et al., 2008), or nuclei in the fission yeast, *S. pombe* (Chang and Martin, 2009).

Most commonly, pulling forces on astral microtubules that originate near the cell cortex or from within the adjacent cytoplasm are critical for centrosome positioning (Goshima and Scholey, 2010; McNally, 2013; Minc et al., 2011). Spindle-cortex interactions are best understood in budding yeast, where two mechanisms work in parallel to pull astral microtubules into the daughter cell (Pearson and Bloom, 2004; Siller and Doe, 2009). A first budding yeast mechanism involves a complex of proteins at the plus ends of astral microtubules that binds a type V myosin, which then transports the astral microtubule along polarized arrays of actin cables. A second mechanism is actin-independent and is mediated by the microtubule motor dynein.

In mammalian cells, dynein is also a major cortical force generator that mediates spindle orientation. The functional importance of dynein for spindle positioning is established in many studies (McNally, 2013; Morin and Bellaïche, 2011; Siller and Doe, 2009). During interphase, dynein can mediate end-on attachment of microtubules to the cell cortex, with force generation coupled to microtubule depolymerization (Laan et al., 2012; Yi et al., 2013). Dynein can also mediate lateral attachment of microtubules to the mitotic cell cortex that generates sliding of microtubule ends along the cortex (Adames and Cooper, 2000; Gusnowski and Srayko, 2011). The cortical distribution of dynein can be regulated by external cues (Morin and Bellaïche, 2011; Siller and Doe, 2009) or by signals from the spindle or the chromosomes (Kiyomitsu and Cheeseman, 2012).

Like in budding yeast, spindle positioning in mammalian cells requires the actin cytoskeleton (Kunda and Baum, 2009), but the underlying molecular mechanism, including possible roles for actin-based motors, is less well understood. An important effect of actin is indirect: F-actin is required to maintain cortical rigidity that prevents end-on microtubule attachments from pulling strands of plasma membrane into the cytoplasm (Kunda and Baum, 2009; Redemann et al., 2010). In some cell types, asymmetric contraction of the cortical actomyosin network may pull on attached astral microtubules, facilitating the positioning of mitotic centrosomes (Rosenblatt et al., 2004). Actin also indirectly affects dynein function by maintaining cortical localization of LGN, a cortical recruitment factor for dynein (Zheng et al., 2013). Finally, prior work has implicated the microtubule-binding myosin Myo10 in spindle positioning (Liu et al., 2012; Toyoshima and Nishida, 2007; Weber et al., 2004); however,

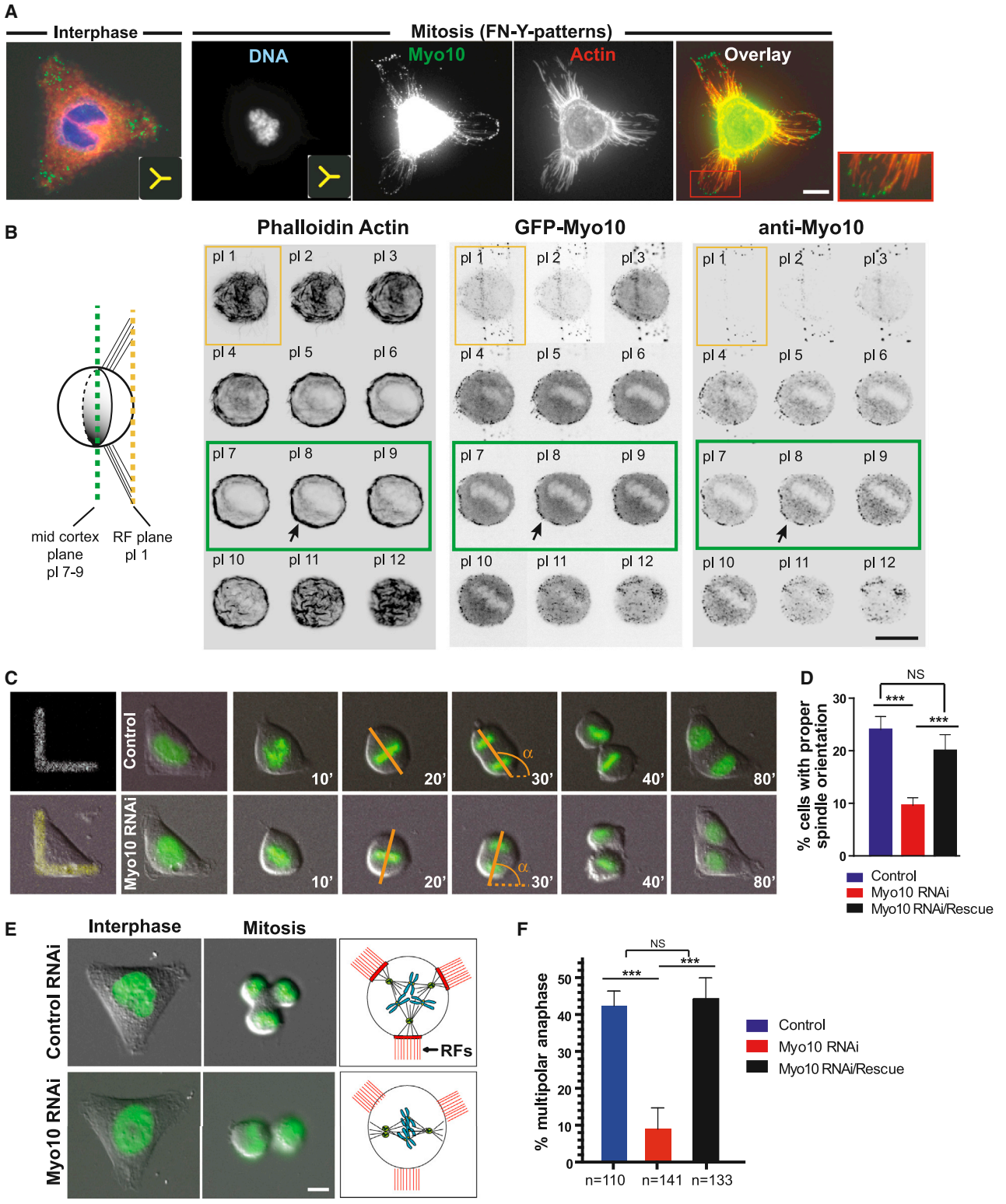

Figure 1. Myo10 Is a Retraction Fiber Protein Required for Centrosome Positioning

(A) Immunolocalization of Myo10 in HeLa cells plated on FN patterns (insets show Y pattern geometry). The red box shows a higher magnification view of Myo10 puncta along retraction fibers. The cell body signal of Myo10 is over-exposed to enable visualization of Myo10 signal at retraction fibers.

(B) Co-enrichment of Myo10 and subcortical actin at the mid-cortex. The left image shows a schematic of a cell plated on a FN-bar pattern, side view. The right image shows a Z-focal plane series (0.5 μm steps) from HeLa cells labeled to detect actin (left), GFP-Myo10 (middle), and Myo10 (right). The yellow and green boxes indicate the planes of retraction fiber (RF) and the mid-cortex, respectively.

(legend continued on next page)

whether Myo10 affects spindle orientation directly or indirectly has been unclear.

Although the molecular mechanisms by which the actin cytoskeleton controls spindle position are not well understood in mammalian cells, significant progress has been made in identifying the relevant actin structures. Mitotic actin-dependent pulling forces originate from retraction fibers, which are cytoplasmic extensions that link rounded mitotic cells to sites of strong cell matrix adhesion (Mitchison, 1992; Théry and Bornens, 2006). Because retraction fibers control spindle orientation, the position of retraction fibers can determine the plane of cell division. This has been demonstrated most elegantly by experiments in which fibronectin micropatterns are used to manipulate the position of retraction fibers (Fink et al., 2011; Théry et al., 2007). In cells with multiple centrosomes, retraction fibers either force cells into multipolar divisions or force the clustering of centrosomes to generate bipolar division, depending on the position of the retraction fibers (Kwon et al., 2008). Thus, mitotic cortical pulling forces concentrate near retraction fibers. Recent work suggests that the assembly of subcortical ''actin clouds'' is required for pulling forces on centrosomes toward retraction fibers. Actin clouds are migrating pools of subcortical actin that extend from the plasma membrane into the cytoplasm, concentrating near retraction fibers (Fink et al., 2011; Mitsushima et al., 2010). Together, these findings suggest a model where cortical regions with attached retraction fibers organize the adjacent cytoplasm by controlling a dynamic subcortical actin network. This network then concentrates force-generating molecules that pull on astral microtubules.

Here, we demonstrate that Myo10, an unconventional microtubule-binding myosin (Weber et al., 2004), is required to orient centrosomes and spindle poles toward actin clouds and retraction fibers. Our data indicate that direct binding to microtubules is critical for Myo10's role in centrosome positioning. By computational image analysis, we demonstrate that Myo10 regulates astral microtubule dynamics and is required for end-on cortical microtubule interactions prior to anaphase. These Myo10 effects are distinct from those of dynein, which we find overlaps with Myo10 for spindle positioning in mammalian cells.

RESULTS

Myo10 Is Required to Orient Centrosomes toward Retraction Fibers

Force generators that orient centrosomes toward the mitotic retraction fiber regions should be present near retraction fibers and/or within the associated subcortical actin clouds; and they should be necessary for orienting centrosomes toward retraction fibers. Ideally, such proteins could also be motor proteins that directly or indirectly bind both actin and microtubules. Motivated by prior work and the results of our genome-wide RNAi screen (Kwon et al., 2008; Toyoshima and Nishida, 2007; Weber et al., 2004), we explore here whether the unconventional microtubule-binding myosin Myo10 is such a force generating protein.

During interphase, Myo10 concentrated at sites of cell-matrix adhesion, often in filopodia (Figure 1A, left), as expected from previous studies (Kerber and Cheney, 2011). During mitosis, Myo10 concentrated in retraction fibers (Figure 1A, right), a finding that was independently confirmed by monitoring GFP-Myo10 localization in three different cell types (Figures 1B and S1A–S1C). In addition to its retraction fiber localization, Myo10 also accumulated asymmetrically at the mid-cortex where asymmetrically positioned subcortical actin clouds assembled (Figure 1B, see planes 7–9).

Experiments using fibronectin (FN) micropatterns demonstrated that Myo10 is required to position centrosomes toward retraction fibers. It is known that retraction fibers control mitotic centrosome positioning in cells with a normal number of centrosomes (Théry et al., 2007). On L-shaped FN patterns, as expected, control U2OS cells oriented their spindles such that the poles were typically positioned between the adhesive regions of the pattern, at an ~135° degree angle with respect to the horizontal portion of the "L" (α, Figure 1C). By contrast, depletion of Myo10 led to significant impairment of spindle orientation with respect to the adhesive pattern (Figures 1C, 1D, and S1D). Ectopic expression of small interfering (si)RNA-resistant GFP-Myo10 rescued this defect, demonstrating the specificity of the knockdown effect (Figures 1D and S1D).

In addition to their role in normal spindle positioning, retraction fibers also control the clustering of multiple centrosomes in cancer cells with centrosome amplification (Kwon et al., 2008). Some cancer cells have the capacity to cluster extra centrosomes (e.g., U2OS cells). In permissive cell types, the clustering of multiple centrosomes provides an independent assay for retraction fiber-mediated centrosome positioning. We therefore induced extra centrosomes in U2OS cells by transient overexpression of the kinase Plk4 (Kleylein-Sohn et al., 2007); these cells undergo bipolar or multipolar divisions, depending (in part) on the position of their retraction fibers (Kwon et al., 2008). When such cells are directly plated onto coverslips, without manipulating the position of retraction fibers, most cells with extra centrosomes cluster their centrosomes and assemble pseudo-bipolar spindles. We found that Myo10 is required for this centrosome clustering, consistent with the hypothesis that it could mediate forces from retraction fiber regions on centrosomes (Figures S1E–S1G).

(C–F) Requirement of Myo10 for spindle orientation (C and D) and the positioning of multiple centrosomes (E and F).

(C) Time-lapse series of control and Myo10-depleted U2OS cells expressing GFP-H2B on FN-L patterns. Time is the minutes from nuclear envelope breakdown (NEBD, t = 0) and α is the angle of the anaphase cell division axis.

(D) Percentage of cells that divide within ±10 degrees of the median angle of 135 degrees, obtained from Figure S1D (α = 135 ± 10, ***$p < 0.003$, non-parametric Student's t test, and three experiments).

(E) Images from a time-lapse series in U2OS cells expressing GFP-H2B that contain extra centrosomes after transient overexpression of Plk4 (Movies S1 and S2): interphase, mitosis, and cartoon of experimental findings (red: RFs).

(F) The percentage of multipolar anaphases in the indicated conditions (***$p < 0.003$, non-parametric Student's t test, and three experiments). The scale bars represent 10 μm. See also Figure S1. All error bars represent mean ± SEM.

Clustering of multiple centrosomes, and the consequent pseudo-bipolar division, can be overridden by directly manipulating the position of retraction fibers. On a Y-shaped FN pattern, cortical forces pulled centrosomes toward the retraction fibers at the tips of the "Y," resulting in tripolar cell division ~45% of the time (Figure 1E, upper, and Movie S1). In this case, interfering with the actin-based pulling forces on centrosomes releases tension, allows pseudo-bipolar spindles to form, and increases the fraction of cells that undergo bipolar divisions. Indeed, after knockdown of Myo10, the cell division axis was decoupled from the position of retraction fibers (Figure 1E, bottom, and Movie S2), and most cells underwent bipolar division (Figure 1F). We note that the requirement of Myo10 for centrosome positioning in mammalian cells cannot be explained by the effect of Myo10 on centrosome number or spindle pole integrity (Figures S1H and S1I) (Kwon et al., 2008; Liu et al., 2012; Toyoshima and Nishida, 2007), unlike what is reported for amphibians (Weber et al., 2004; Woolner et al., 2008). Thus, multiple assays suggest that Myo10 is required for cortical pulling forces to position centrosomes at or near retraction fibers.

Myo10 Is Not Required for Normal Cell-Matrix Adhesion or for Retraction Fiber Assembly

The function of Myo10 in mitotic centrosome positioning is independent of the requirement for Myo10 in retraction fiber assembly, mitotic cell rounding (Figures 2A and S2A–S2D), and assembly of subcortical actin (Figures 4, S4, 5, and S5; see next section). Myo10 depletion led to no detectable defects in mitotic cell rounding (Figure S2D), in contrast with one previous report (Toyoshima and Nishida, 2007), and no detectable defects in the morphology or organization of subcortical actin.

Because Myo10 transports $\alpha5\beta1$ integrin along filopodia via its FERM domain (Zhang et al., 2004), we examined the effect of Myo10 depletion on integrin signaling (Figures 2B and 2C). Both the Src and FAK kinases were fully activated in multiple cell lines after Myo10 depletion (Figures 2B, 2C, and S2E), although a small, but reproducible, delay in FAK activation was evident at the 1 hr time point (Zhang et al., 2004). Likewise, in cells plated on FN micropatterns, recruitment of paxillin to focal adhesions was also unaffected by Myo10 depletion (Figures 2D and 2E). Thus, Myo10 depletion does not detectably affect retraction fiber assembly, mitotic rounding, or integrin signaling.

Microtubule Binding by Myo10 Is Required for Centrosome Positioning

Myo10 is a processive actin motor that binds microtubules through the MyTH4 domain located in its tail (Kerber and Cheney, 2011; Weber et al., 2004) (Figure S1B). Although the motor domain of Myo10 (Myo10-HMM) was sufficient for its localization to retraction fibers (Figures S1B and S1C), expression of the isolated motor domain did not rescue the centrosome-clustering defect in Myo10 knockdown cells (Figure S1E). Likewise, the Myo10 tail domain (PH-MyTH4-FERM) on its own was not able to complement the depletion of Myo10 (Figure S1E). Centrosome positioning by Myo10, therefore, requires both its actin-binding motor and microtubule-binding tail domains.

Other interaction partners of the Myo10 tail could also be important for centrosome positioning (Kerber and Cheney, 2011; Liu et al., 2008; Woolner and Bement, 2009). This not only includes FERM domain interactions with integrins, but also microtubule regulators (Katanin and TPX2), actin regulators (Ena and VASP), and regulators of cell polarity (aPKC). Previous studies were not able to discriminate the effects of microtubule-binding from the effects of these other interactions (Woolner and Bement, 2009) (Figure S1E). However, a recent X-ray structure identified specific residues (K1647 and K1650) within the MyTH4 domain that are essential for direct binding to the acidic carboxy-terminal tubulin tail (Hirano et al., 2011; Wei et al., 2011; Wu et al., 2011) (Figure S3A, asterisks in the red box). This enabled us to generate the Myo10-KK-DD point mutation construct (Figures 3A and S3A) that specifically disrupts microtubule lattice-binding without altering the interaction of Myo10 with FERM domain-binding cargo (Hirano et al., 2011).

Imaging experiments demonstrated that the Myo10 microtubule-binding site mutations, including deletions that completely lack the MyTH4 domain, had no effect on Myo10's localization to filopodia or retraction fibers (Figures 3A and 3B). However, complementation with siRNA-resistant constructs demonstrated that Myo10 microtubule-binding is critical for centrosome positioning (Figures 3C and S3B–S3D). In cells plated on FN-L patterns, neither MyTH4 deletion nor the Myo10-KK-DD point mutant rescued the spindle orientation defect resulting from Myo10 knockdown (Figures 3C and S3C). The failure of the mutants to complement cannot be explained by defects in expression or localization (Figures 3B, upper, and S3B). Similar results were obtained for the microtubule-binding deficient mutants in the multiple centrosome-clustering assay (Figures 3B, bottom, and S3D). Collectively, these data suggest that direct microtubule lattice-binding by Myo10 is critical for its ability to position centrosomes in response to cortical forces (Figure S3E).

Myo10 Is Required for Spindle Orientation Relative to Subcortical Actin Clouds

Although localization of subcortical actin clouds is strongly correlated with centrosome positioning (Fink et al., 2011), the molecular connection between the actin clouds and the astral microtubules and/or centrosomes is not known. To test the idea that Myo10 is this link, we first quantified its localization relative to the position of the actin clouds. The density of Myo10 at the cell cortex corresponded to the distribution of the underlying subcortical actin clouds (Figures 4A–4D). This was clearly apparent in HeLa cells plated on bar-shaped FN patterns that accentuate the asymmetrical accumulation of the actin clouds at the mid-cortex (Figures 4A–4D).

Next, we investigated whether Myo10 is required to form the subcortical actin clouds. F-actin was visualized by phalloidin staining in cells plated on FN-bar patterns (Figures 4E–4G). As expected (Fink et al., 2011), subcortical actin concentrated on one (unipolar distribution) or both (bipolar) sides of the FN bar in the majority (~80%) of control cells, but was homogenously distributed in the remaining 10%–20% of the cells (Figures 4E, 4F, S4A, and S4B). Importantly, depletion of Myo10 had no effect on either the formation or polarization of subcortical actin (Figures 4F and S4D), but led to a ~4-fold decrease in the ability of cells to align their spindles with unipolar subcortical

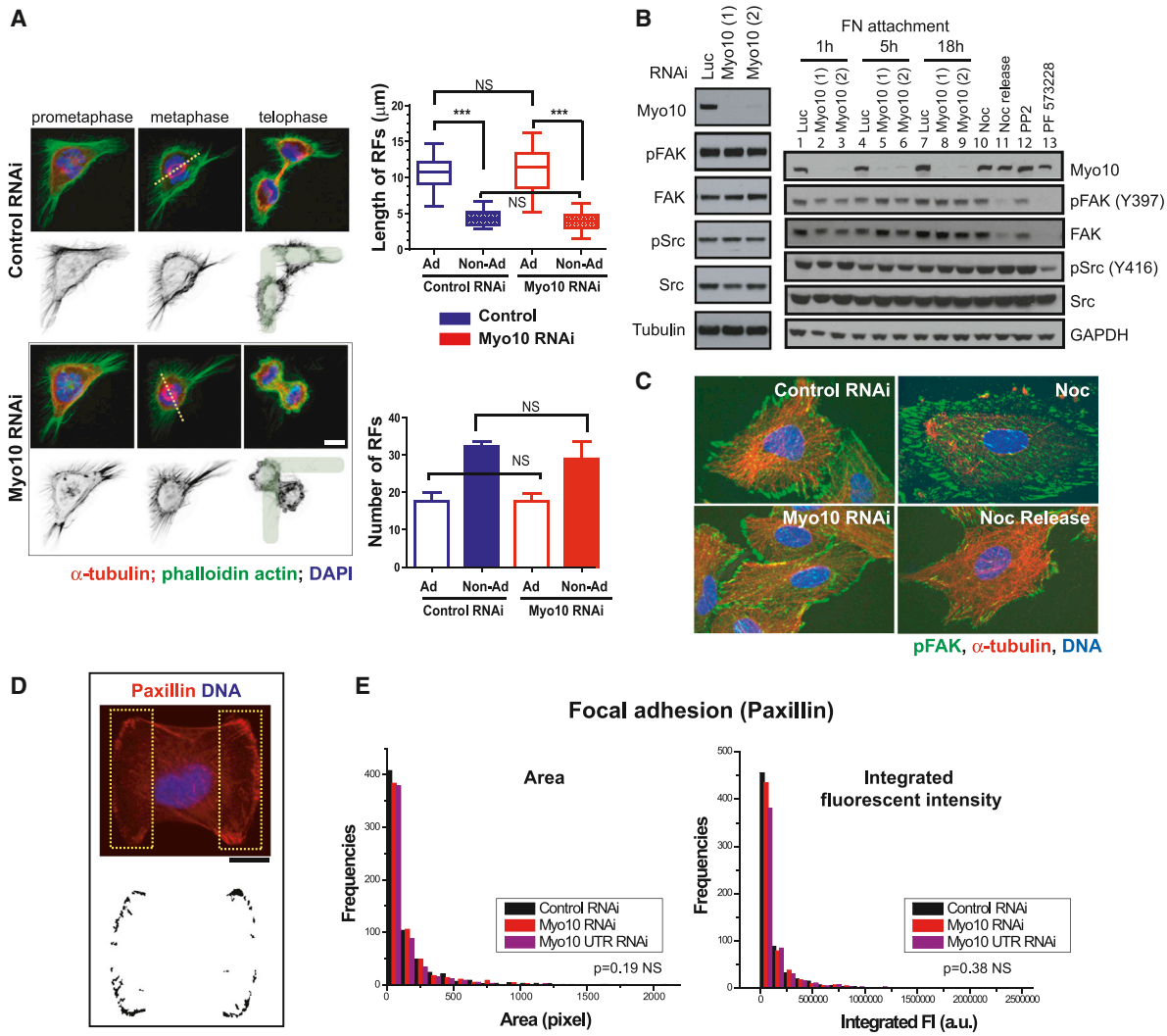

Figure 2. Myo10 Inhibition Does Not Disrupt Retraction Fiber Formation or Cell Adhesion

(A) The left image has immunofluorescence images showing normal retraction fiber (RF) morphology during prometaphase, metaphase, and telophase of control or Myo10-depleted HeLa cells plated on L-patterns. The cells were stained for microtubules, actin, and DNA. The dotted lines show the pole-to-pole spindle axis. The right image shows no difference in length (top) and number (bottom) of RFs in both adhesive (Ad) and non-adhesive (Non-Ad) regions upon control or Myo10 RNAi (n = 20 cells from three experiments, ***p < 0.0001, and non-parametric Student's t test, not significant: NS) (mean ± SEM).

(B and C) Comparable level of activation and distribution of downstream effectors of integrin-mediated adhesion signaling after Myo10 depletion in RPE-1 cells. The two independent Myo10 siRNAs were used.

(B) Western blots showing steady-state Src and FAK activation (left, 24 hr post-attachment) and the kinetics of activation (right, 1, 5, and 18 hr post-attachment). The positive controls show decreased FAK and Src activation after treatment with Src (PP2) or FAK (PF573228) inhibitors or by microtubule-regrowth-mediated focal adhesion disassembly, Nocodazole (Noc) release (Ezratty et al., 2005).

(C) Immunofluorescence images of pFAK (Y397), α-tubulin, and DNA staining in control or Myo10-depleted cells. The Noc treatment (microtubule-depolymerization-induced focal adhesion assembly) and 1 hr post-Noc release (microtubule-regrowth-mediated focal adhesion disassembly) serve as positive and negative controls for FAK activation.

(D and E) No defects in focal adhesion protein distribution in control or Myo10-depleted RPE-1 cells plated on FN-H patterns.

(D) Immunofluorescence image of a cell stained for paxillin and DNA 5 hr post-attachment. The two yellow dotted boxes corresponding to the adhesive surfaces of cells on the H pattern were segmented (bottom image) for paxillin signal.

(E) Corresponding quantitation of the area and integrated fluorescence intensity of paxillin islands (D) in the indicated conditions (n = 15 cells per condition from two experiments). The scale bar represents 10 μm. See also Figure S2.

actin (Figures 4G and S4C). Thus, Myo10 is essential to orient centrosomes with subcortical actin, but is not required to assemble these actin structures (Figure 4E).

Live-cell imaging confirmed a key role for Myo10 in coordinating centrosome movement with the local positioning of actin clouds (Figures 5 and S5). Subcortical actin dynamics were visualized by GFP-tagged calponin homology (CH) domain of utrophin (GFP-Utr-CH), a fluorescent F-actin binding protein (Mitsushima et al., 2010; Woolner et al., 2008). Imaging of cells expressing GFP-Utr-CH and mCherry-tubulin

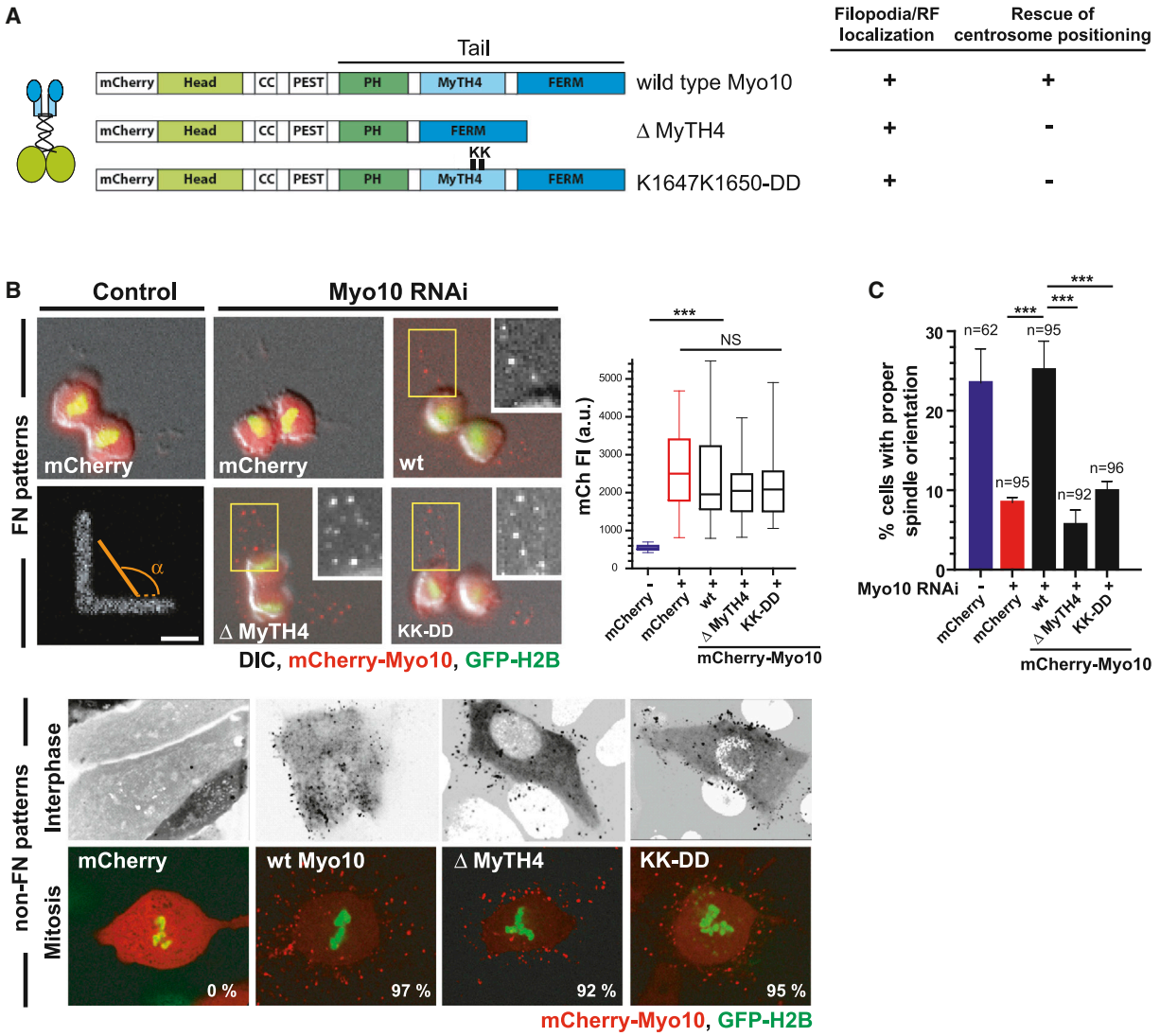

Figure 3. Direct Binding of Myo10 to Microtubules Is Required for Centrosome Positioning

(A) Schematic of mCherry-tagged Myo10 constructs used in siRNA-rescue experiments.

(B) Expression and localization of the indicated mCherry-tagged Myo10 constructs in cells expressing GFP-H2B. The top panels are from time-lapse images of control and Myo10-depleted U2OS cells on FN-L patterns. The insets have enlarged views showing retraction fiber localization of Myo10 constructs in yellow boxed regions. The right graph shows the corresponding mCherry fluorescence quantitation. The bottom image shows the normal localization of the indicated Myo10 constructs to filopodia (top: inverted images) and retraction fibers (bottom) in the cells with extra centrosomes. The percentage of cells with proper Myo10 localization is indicated.

(C) Requirement of Myo10 microtubule-binding, but not its cargo-binding, for spindle orientation on FN-L patterns. The spindle orientation analysis was done as in Figures 1C and 1D (***$p < 0.001$, non-parametric Student's t test, and three experiments). The scale bar represents 10 μm (mean ± SEM). See also Figure S3.

showed that, during oscillatory spindle movements, spindle poles move toward subcortical actin clouds after a time lag (Figure 5A, left, and Movie S3), as reported (Fink et al., 2011). The correlated pole movement toward actin clouds was confirmed in kymographs (Figures 5B and S5). Strikingly, spindle pole movement toward actin clouds was largely dependent upon Myo10 (Figures 5A, 5B, and S5), consistent with the above analysis of fixed cells (Figures 4E–4G and S4). Although Myo10 depleted cells had no detectable defects in the polarization and movement of subcortical actin clouds (Figure 5A), they did show a significant decrease in the frequency and velocity of pole movement toward actin clouds (Figures 5B, middle, S5B, and S5C and Movie S3). This effect of Myo10 depletion was mirrored by that of Arp2/3 inhibition, which completely disrupts actin clouds (Figures 5A, 5B, S5B, and S5C and Movie S3) without affecting retraction fibers (Mitsushima et al., 2010). Actin clouds and Myo10 are also required for spindle orientation in cells plated on FN-L patterns (Figure 5C). Thus, Myo10 is not essential for actin cloud assembly, but is vital for forces that move centrosomes toward actin clouds during spindle oscillations and spindle orientation.

The Effect of Actin and Myo10 on Astral Microtubule Dynamics

Despite numerous studies on the role of the actin cytoskeleton in spindle orientation (Kunda and Baum, 2009; Sandquist et al., 2011), how the actin cytoskeleton affects astral microtubule dynamics during mitosis has not been systematically examined. To determine the effect of actin disassembly or Myo10 knockdown on microtubule dynamics, we used spinning disc confocal microscopy of cells expressing GFP-EB3, a microtubule plus end binding protein that forms comets on growing microtubules (Figures 6 and S6). Comet trajectories were recorded using the plusTipTracker software (Applegate et al., 2011; Matov et al., 2010), enabling unbiased analyses of tens of thousands of microtubules for a given condition. The method yields direct measurements of microtubule growth speeds and growth lifetimes and includes an algorithm to infer shrinkage events from spatially collinear growth events (Figure 6A and Movie S4). To achieve high spatio-temporal resolution, we employed single focal plane imaging at the mid-cortex in Z near the spindle poles, where actin clouds accumulate. Because Myo10 is essential for mitotic centrosome positioning in multiple cell lines (Figures 1C–1E, S2A–S2C, 3, 4E–4G, and 5), we selected RPE-1 cells, whose flat morphology enabled robust automated analysis of microtubule dynamics.

After actin depolymerization with Latrunculin A (LatA), astral microtubules grew and shrank significantly faster, and had shorter growth lifetimes, than in control cells (Figures 6B and S6A; permutation t test, $^{***}p < 0.0001$, and $^{**}p < 0.02$). This effect was also evident when pooling the data for control and experimental conditions, followed by unbiased segmentation using K-means clustering of populations of cells with highly dynamic (fast-growing/shrinking and short lifetime-high frequency switching), and less dynamic (slow-growing/shrinking with longer lifetime-low frequency switching) microtubule behavior (Figure 6C). The increase in microtubule dynamics was dependent on the dose of LatA (Figure S6B). These findings thus reveal that interactions with the actin cytoskeleton suppress the dynamicity of astral microtubules during mitosis.

Next, we determined the effect of Myo10 depletion on astral microtubule dynamics (Figures 6B, 6C, and S6A). Overall, Myo10 knockdown (red) increased astral microtubule dynamics in a manner that was similar to that of LatA treatment (yellow), although to a slightly lesser extent. By contrast, treatment of cells with blebbistatin (green), a specific myosin II ATPase inhibitor, had little effect on microtubule growth and shrinkage speeds, despite the decrease in microtubule growth lifetime (Figures S6A and S6B). Thus, the distinct effect of Myo10 on microtubule dynamics cannot be simply explained by a general defect in actomyosin contractility.

The effect of Myo10 on astral microtubule dynamics requires microtubule-binding. After Myo10 knockdown, add-back of the Myo10 point mutant (KK-DD, open red circles), which is deficient in microtubule-binding, had an effect on astral microtubule dynamics that was similar to that of the Myo10 knockdown (Figures 6D and S6C). Moreover, Myo10 knockdown predominantly affected astral microtubule dynamics (Figure S6D): Kymograph analysis of spindle microtubules, where single particle tracking of comets is inaccurate, showed no detectable effect of Myo10 knockdown on microtubule growth. These results suggest that Myo10 directly mediates interactions of astral microtubules with the actin network in vivo and modulates their dynamics.

The Effect of Actin and Myo10 on Astral Microtubule Cortical Interactions

Next, we determined whether Myo10 is required for astral microtubule ends to interact with the cell cortex. We developed software to make quantitative measures of cortical-microtubule interactions during mitosis. We analyzed the lifetime of EB comets in a 1 μm wide band from the cell boundary (Figure 6E; see Supplemental Information for details). The microtubule cortical dwell time was measured as the time that the EB3 comet persisted within a 200 nm radius around each microtubule trajectory end point. Actin disruption or Myo10 depletion diminished the cortical dwell time during metaphase (Figure 6E, bottom left). This effect was not due to faster dissociation of EB3 from microtubule plus ends (Figure S6E; see Supplemental Information for details), validating the use of EB3 to visualize microtubule ends and measure cortical dwell time. LatA-treated or Myo10-depleted cells also exhibited significantly higher frequency of contact between astral microtubules and the cell cortex relative to control cells (Figures 6E, upper, and S6F), consistent with the increased microtubule dynamicity in these cells (Figure 6C). Importantly, cells that express the microtubule-binding deficient point mutants (Myo10-KK-DD) displayed similar microtubule-cortical interactions as LatA-treated or Myo10 knockdown cells (Figure 6E, bottom right). Together, these results show that the microtubule-binding activity of Myo10 facilitates interactions between astral microtubules and the cell cortex.

Overlapping Roles of Myo10 and Dynein

We observed two modes of astral microtubule interactions with the cell cortex that are broadly similar to findings previously reported in budding yeast (Adames and Cooper, 2000; Pearson and Bloom, 2004). Some astral microtubules approached the cell edge directly, before stalling or undergoing catastrophe (hereafter referred to as ''end-on microtubules,'' Figure 7A, blue), whereas others appeared to slide along the cell edge (hereafter referred to as ''lateral sliding microtubules,'' red). We developed software that distinguishes between these two types of microtubules (Figures 7A and S7A and Movie S5). A cortical microtubule was defined as undergoing lateral sliding when it grew for >0.7 μm within the 1 μm wide cortical band and maintained a terminal direction of motion roughly parallel to the cell edge (Figure S7A; see Supplemental Information for details). All other cortical microtubules that traveled a significant distance within the cortical band (>0.3 μm) were defined as end-on interacting. Consistent with observations in *C. elegans* (Gusnowski and Srayko, 2011), we observed few lateral sliding events in pre-anaphase cells, when the spindle pole is relatively far from the cell cortex; however, lateral sliding became relatively frequent post-anaphase, when the poles are in close proximity to the cortex. To directly compare the impact of Myo10 and dynein inhibition on these different modes of cortical-microtubule contact, we examined pre- and post-anaphase cells, in the latter case, our analysis was restricted to cells that had a comparable pole-to-cortex distance (3–4 μm).

Unlike Myo10 (Figure 6E), the cortical pool of dynein did not affect the cortical dwell time of astral microtubules during

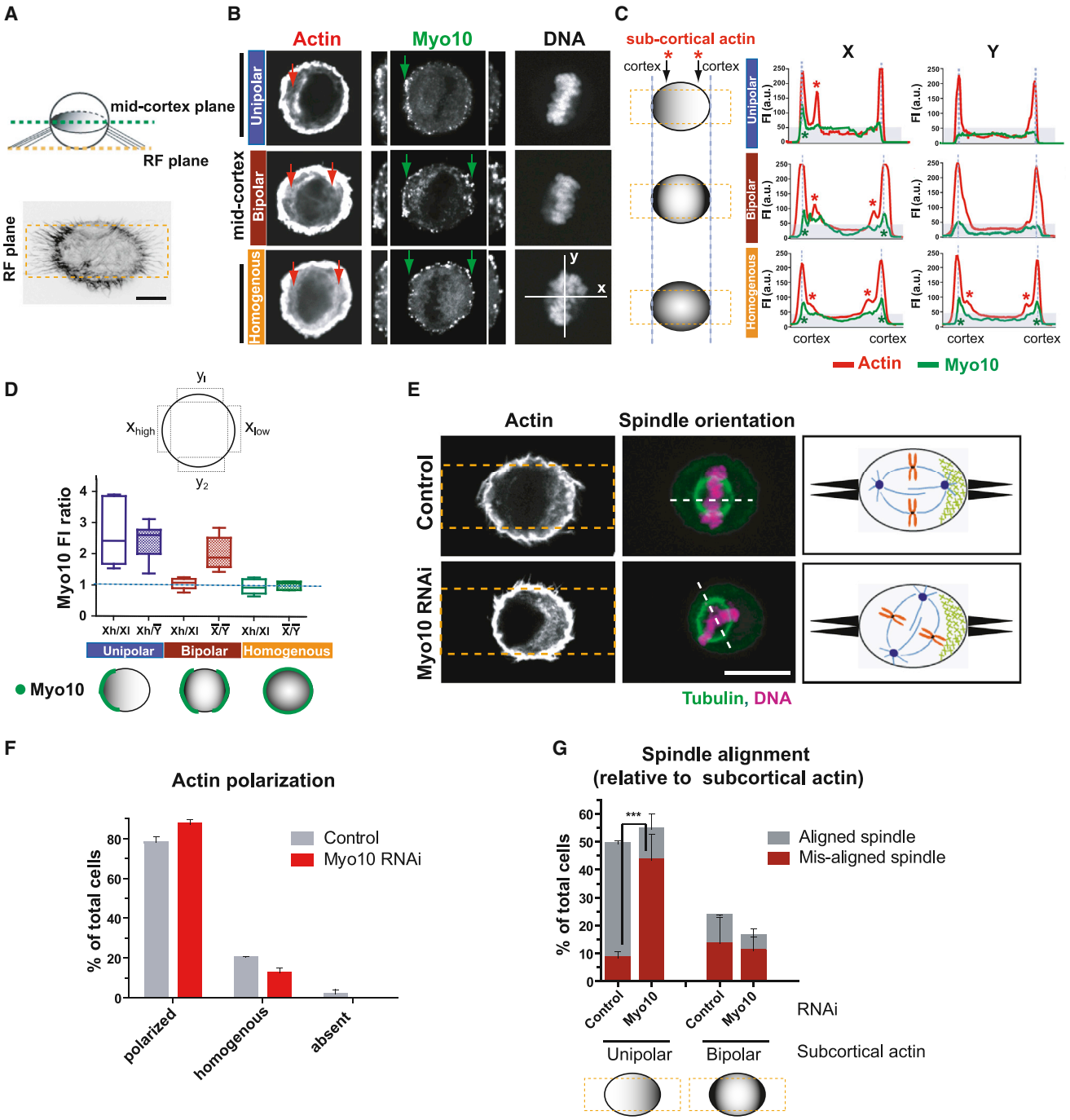

Figure 4. Myo10 Is Required for Spindle Orientation toward Polarized Subcortical Actin

(A–D) Asymmetric accumulation of Myo10 at the mid-cortical plane of the mitotic cortex is correlated with the asymmetric distribution of subcortical actin.

(A) The top image shows a schematic of a cell plated on FN-bar pattern from a side view. The bottom image shows the phalloidin actin staining of a HeLa cell from the retraction fiber (RF) focal plane.

(B) Representative images of cells where actin and Myo10 are concentrated on one side of the cell (unipolar), both sides (bipolar), or homogeneously distributed. Note that Myo10 accumulates near the cell boundary, at the base of the retraction fibers (see green arrows and insets with enlarged view of both sides of the cell).

(C) Fluorescence line scans of actin (red) and Myo10 (green) along x axis (left) or y axis (right) of the bar pattern from (B). The red and green asterisks show sites of high accumulation of subcortical actin and Myo10, respectively (see also corresponding arrows in B).

(D) Schematic for the Myo10 fluorescent intensity (FI) quantitation shown below. The plot shows FI ratios of Myo10 in the indicated regions from cells classified based on the distribution of subcortical actin in (B) and (C). The open boxes measure asymmetry along the x axis of the pattern; hatched boxes measure the asymmetry of x over y axis of the pattern (n = ~15 line scans per category from two experiments). The bottom image shows a cartoon summarizing observations.

(E–G) Myo10 does not affect the assembly or distribution of subcortical actin clouds, but is required for spindle alignment relative to subcortical actin.

(legend continued on next page)

metaphase (not significant [NS], permutation test of the medians from four experiments; control cells: n = 34 cells and 354 microtubules; and LGN RNAi: 23 cells and 240 microtubules), consistent with a previous report (Samora et al., 2011). In this experiment, the cortical pool of dynein was inhibited by knockdown of LGN, a cortical recruitment factor for dynein (Figure 7B) (Kiyomitsu and Cheeseman, 2012; Morin and Bellaïche, 2011). In this condition, we also did not detect any decrease in cortical dwell times during anaphase (Figure S7D). However, we did find that cortical dynein was required for anaphase lateral sliding events (Figures 7C–7E and Movie S5), as documented in other systems (Adames and Cooper, 2000; Pearson and Bloom, 2004). The conclusion that dynein is specifically required for promoting lateral sliding is robust to small-scale alterations of the lateral sliding classification parameters in our automated analyses (Figures S7B and S7C). Importantly, this effect cannot be explained by a decrease in the density of cortical EB3 comets (Figure S7E). Unlike dynein, Myo10-depletion did not impair end-on or lateral sliding microtubule attachments during anaphase (Figures 7D, 7E, and S7D and Movie S5). Thus, Myo10 and dynein have distinct effects on microtubule-cortical interactions: Myo10 is required for end-on microtubule attachment prior to anaphase (Figure 6), and dynein is required for lateral sliding of microtubules during anaphase.

To determine if the Myo10 and dynein mechanisms act in parallel, we examined the individual and combined effects of Myo10 and LGN knockdown on spindle orientation (Figure 7F) and on the clustering of centrosomes in cells with centrosome amplification (Figure 7G). Consistent with parallel action, double knockdown of Myo10 and LGN had an additive effect, randomizing spindle orientation, as compared to the individual knockdowns (Figure 7F, right, compare brown line with arrow to red or green lines). An additive effect of Myo10 and LGN knockdown was also observed using the centrosome-clustering assay (Figures 7G and S7F). Finally, Myo10 knockdown did not impair dynein cortical localization, and LGN knockdown similarly did not alter the cortical distribution of Myo10 (Figures 7C, S7G, and S7H). These results define two overlapping pathways for positioning centrosomes during mitosis in human cells: a Myo10-dependent pathway and an LGN/dynein/dynactin-dependent pathway.

DISCUSSION

Requirement of Myosin-10 for Spindle Pole Movement toward Retraction Fibers and Subcortical Actin Clouds

Here, we document that the microtubule-binding myosin Myo10 is required for actin-dependent forces on the centrosome in human cells during mitosis. Our data suggest that Myo10 is the major actin-based force generator that pulls astral microtubules toward retraction fibers and subcortical actin clouds. First, Myo10 concentrates in the cortical region around these actin structures. Second, Myo10 is functionally important to position spindle poles relative to these structures. The fact that Myo10 is not required for the assembly or dynamics of retraction fibers and actin clouds suggests that Myo10 is specifically required for the generation of pulling forces toward these structures. Because retraction fibers control the polarization of actin clouds, we propose that these structures form a continuous actin network, through which Myo10 motors orient astral microtubules. Indeed, Myo10 is a processive motor capable of walking on individual actin filaments and on actin bundles, that also has the capacity to switch between filament tracks (Kerber et al., 2009; Nagy et al., 2008; Nagy and Rock, 2010; Sun et al., 2010). Thus, Myo10 is well suited for transporting microtubules through variously shaped actin structures.

We can envision several ways in which the Myo10 biochemical activities may be harnessed to position centrosomes near retraction fibers. The simplest model would be direct transport of astral microtubules through the subcortical actin clouds toward the base of the retraction fibers, driven by the interaction of Myo10 with the microtubule lattice. This model requires that the subcortical actin clouds have a net polarity, which has not been tested. This is, however, plausible, as the actin clouds are assembled in a manner that requires the Arp2/3 complex (Mitsushima et al., 2010), in common with polarized actin in lamellipodia (Pollard and Borisy, 2003). In sea urchin eggs, cytoplasmic pulling forces on astral microtubules increase with increasing microtubule length (Minc et al., 2011). By binding to the microtubule lattice, in principal, the numbers of bound Myo10 molecules could be proportional to microtubule length, thus generating length-dependent pulling forces on centrosomes. Finally, Myo10 may facilitate the action of dynein or other, unknown, force generators, by anchoring microtubules to the actin structures associated with retraction fibers.

The Requirement for Microtubule Binding by Myo10

Our data demonstrate that the mitotic function of Myo10 in centrosome positioning depends, almost completely, on its ability to bind the microtubule lattice. Several studies suggest that Myo10 links actin and microtubules, based on deletions that encompass the MyTH4-FERM domain (Weber et al., 2004; Woolner et al., 2008). However, this prior work could not distinguish compromised microtubule-binding from the loss of other cargo that binds the FERM domain. Here, we make this distinction by utilizing the Myo10 point mutations that specifically disrupt microtubule-binding without altering other known cargo binding (Figure 3) (Hirano et al., 2011; Wei et al., 2011).

We also considered the possibility that Myo10 interacts indirectly with microtubules through EB-family microtubule plus end-binding proteins. *Drosophila* myosin XV, a related MyTH4-FERM domain myosin, binds to EB1 through its MyTH4-FERM domain and other microtubule regulators through its FERM domain (Liu et al., 2008). We also noticed that many Myo10 homologs contain several potential EB1 binding, SxIP-like motifs (Honnappa et al., 2009) within the MyTH4 domain (Figure S3A). However, a construct containing point mutations in all of the

(E) Immunofluorescence images of control or Myo10-depleted cells plated on FN-bar patterns (yellow dashed boxes) and stained for actin, tubulin, and DNA. The schematic summary is shown in the right box: retraction fibers (black protrusions) and subcortical actin (green mesh). The scale bar represents 10 μm.

(F) Percentage of cells with the indicated distribution of subcortical actin with control or Myo10 RNAi treatment (mean ± SEM).

(G) Percentage of cells exhibiting aligned or misaligned spindle with unipolar or bipolar actin clouds (n = ~100 cells from three experiments, ***$p < 0.001$, and non-parametric Student's t test. See Figure S4C for data including detailed category of actin cloud organization (mean ± SEM). See also Figure S4.

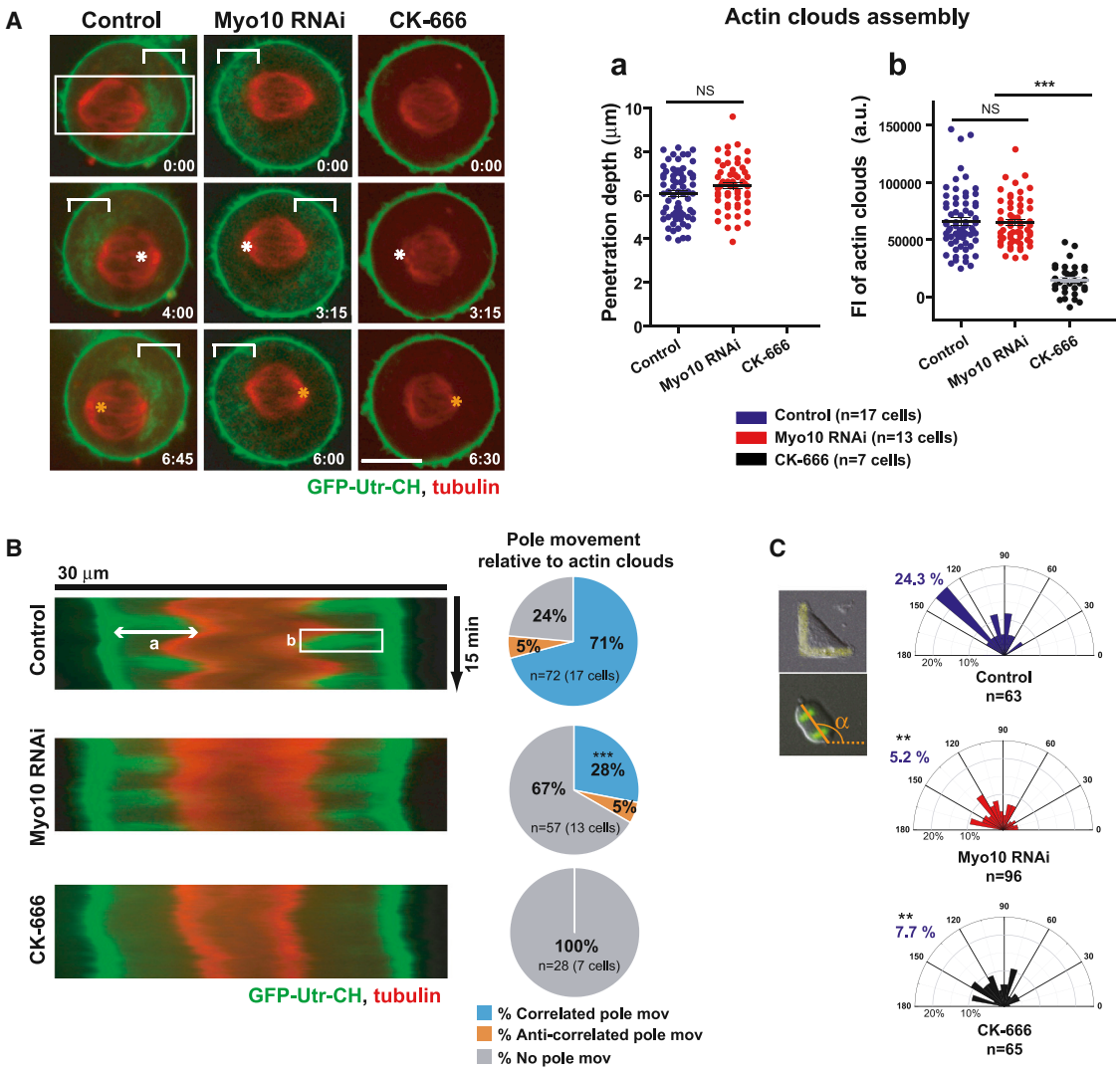

Figure 5. Myo10 Is Not Required for the Assembly or Dynamics of Actin Clouds but Is Required to Pull Centrosomes toward Subcortical Actin Clouds

(A) Time-lapse images of control, Myo10-depleted, or CK-666 (100 μM, Arp2/3 inhibitor)-treated HeLa cells expressing GFP-Utr-CH and Cherry-tubulin (see Movie S3). Equatorial planes were imaged at 15 s intervals during metaphase spindle oscillations (time, min: sec). The white and orange asterisks (middle and bottom) show the positions of spindle pole at the previous time point (top and middle). The white brackets show actin clouds. The right graphs show the penetration depth (a) and integrated fluorescent intensity (b) of actin structures quantified from kymographs, as shown in (B) (***$p < 0.0001$, non-parametric Student's t test, and three experiments). The scale bar represents 10 μm.

(B) A decrease in the coordinated spindle pole movements toward actin clouds in Myo10-depleted cells. The left image shows kymographs of actin clouds (green) and spindle poles (red) generated from the region indicated by the white boxes (70 pixel in width shown in A) along the spindle axis in the indicated conditions. Pie charts at right show the spindle pole movements relative to actin cloud accumulation that were classified as correlated (blue, pole moves toward actin clouds), anti-correlated (orange, pole moves against actin clouds), or no (gray) movement, as described in Figures S5A and S5B. The percentage of pole movements in each category is shown in the indicated conditions (***$p < 0.003$, non-parametric Student's t test, and three experiments).

(C) Requirement of Myo10 and actin clouds for spindle orientation in HeLa cells plated on FN-L patterns. The imaging and analysis were done as in Figures 1C and 1D (**$p < 0.01$, non-parametric Student's t test, and two experiments ±SEM). See also Figure S5.

Myo10 SxIP motifs nonetheless rescued the centrosome-positioning defect in Myo10 knockdown cells to near completion (~18% as compared with 15% multipolar spindles for the controls, as in Figure S3D). Although we do not exclude a contribution from the EB protein binding to Myo10, our analysis indicates that microtubule lattice-binding is the primary mechanism underlying Myo10-dependent centrosome positioning.

Actin and Myo10 Regulate Dynamics and Cortical Attachment of Microtubules during Mitosis

Using computational image analysis, we show that actin and Myo10 decrease microtubule dynamicity and promote end-on cortical-microtubule interactions prior to anaphase (Figures 6 and S6). The similarity in the effect of LatA treatment and Myo10 knockdown, together with the fact that Myo10 does not

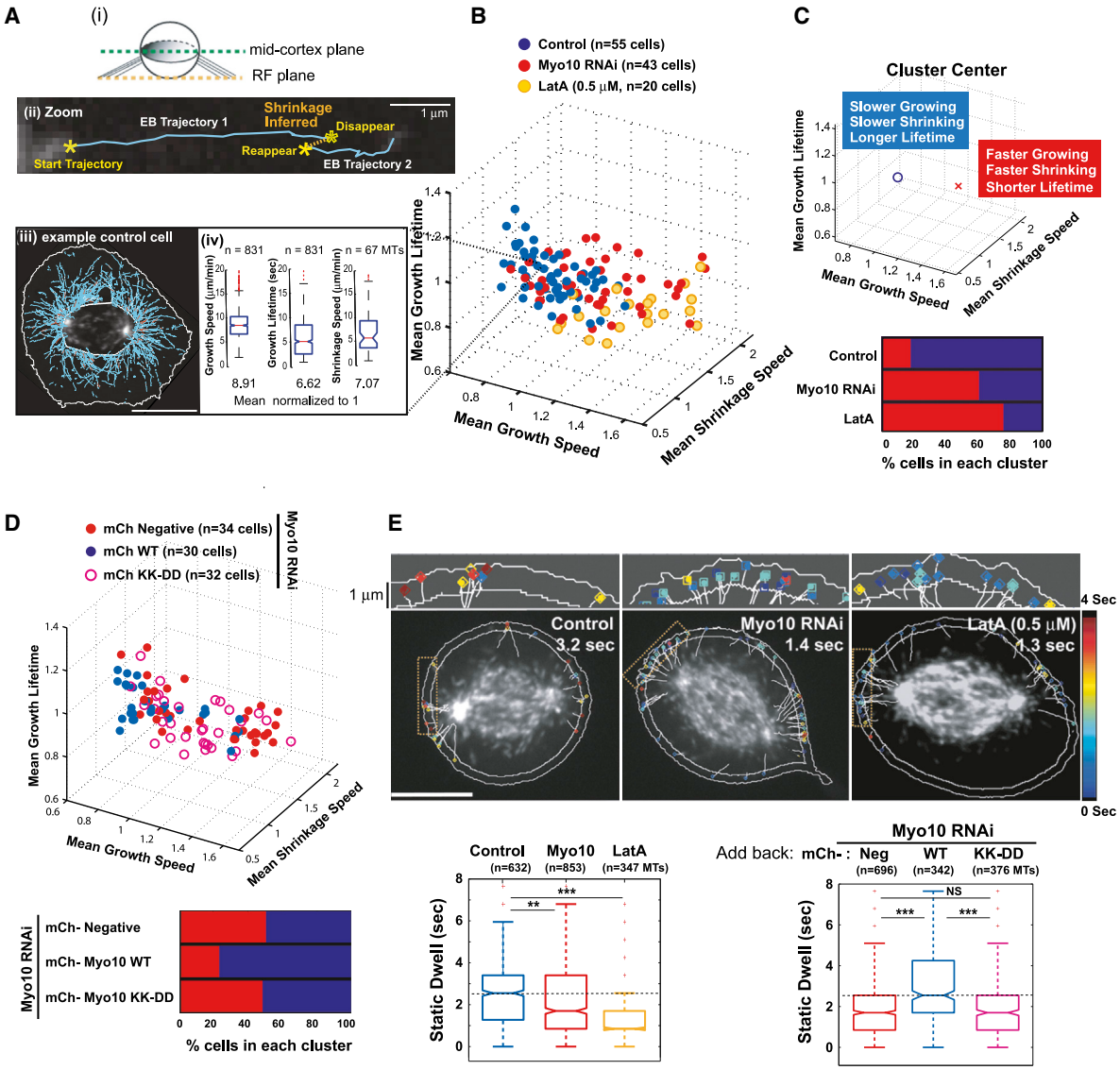

Figure 6. Actin or Myo10 Suppresses Microtubule Dynamicity near the Cell Cortex prior to Anaphase

(A–C) Myo10 depletion increases microtubule growth rates, shrinkage rates, and numbers of short-lived microtubules (RPE-1 cells expressing GFP-EB3).

(A) (i) In the schematic, the images were taken from the mid-cortical plane of a rounded mitotic cell. (ii) The zoomed image of a microtubule shrinkage event (orange dotted line) inferred from the linkage of two collinear EB3 comet trajectories (Movie S4). (iii) Representative image of a control cell with EB3 comet trajectories (solid cyan lines). (iv) Distributions of the indicated microtubule parameters extracted from the representative control cell shown in (iii). Data were obtained from cells with a metaphase chromosome configuration as judged by DIC.

(B) 3D plot of microtubule growth speed, shrinkage speed, and growth lifetime obtained from control cells (blue), cells depleted of Myo10 (red), or cells treated with LatA (yellow). Each data point represents the average microtubule parameters quantified from the entire astral microtubule population per cell from five experiments. The per cell values for each parameter were normalized by the mean value of the per cell control distribution for a given experimental day. The mean control values were normalized to 1 from measured values of 9.6 ± 1.0 μm/min (growth speed), 6.8 ± 1.0 μm/min (shrinkage speed), and 6.1 ± 0.5 s (growth lifetime).

(C) Both actin disruption and Myo10 depletion result in increased microtubule dynamicity. The top graph shows that K-means clustering of data shown in (B) distinguishes two separate populations of cells that possess different characteristic microtubule dynamics (see Supplemental Information for details). Each cell belongs to a respective cluster, "O" (less dynamic) or "X" (highly dynamic). The bottom graph shows the percentage of cells possessing highly dynamic (red, cluster center X) or less dynamic (blue, cluster center O) microtubules after the indicated treatment from (B).

(D) Requirement of Myo10 microtubule-binding to regulate astral microtubule dynamics. The top graph shows a 3D plot of indicated microtubule parameters obtained from Myo10-depleted cells expressing mCherry (mCh)-tagged wild-type Myo10 or the KK-DD mutant. The mCh-negative Myo10-depleted cells (closed red circles) serve as the negative control. The mean wild-type Myo10 rescue values were normalized to 1. The bottom graph shows the data presented as in Figure 6C (two experiments).

(E) Myo10-dependent cortical interactions of astral microtubules. The top image shows the automated measurements of static dwell time within the 1 μm cortical band. The microtubule tracks are shown as white lines and the dwell time is presented as colors from a heatmap. The bottom box plots show the static dwell time (sec) of astral microtubules (MTs) in the indicated conditions from five (left) and two (right) experiments (***$p < 0.00001$, **$p < 0.006$, and permutation test of the medians). The scale bars represent 10 μm. See also Figure S6.

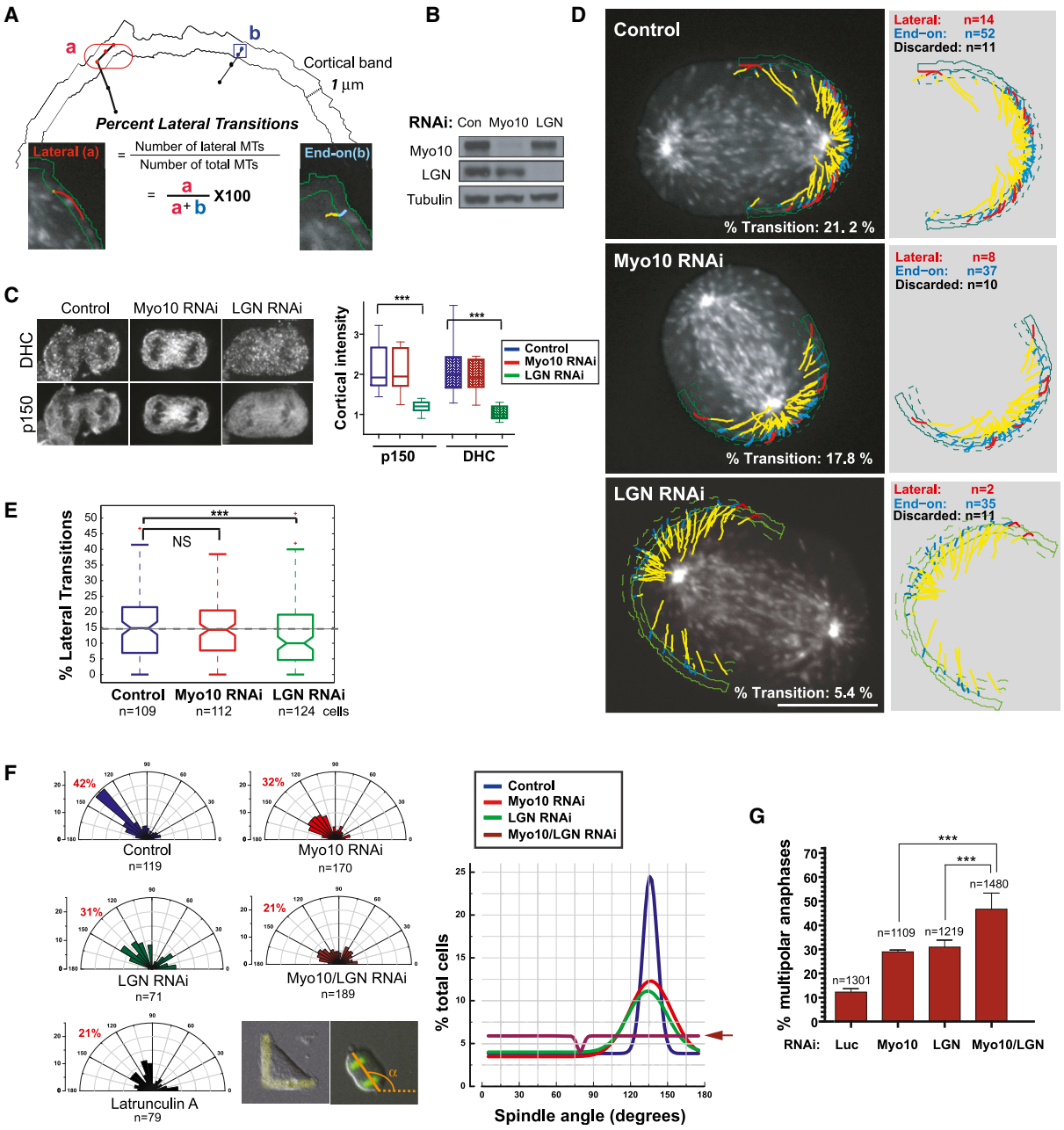

Figure 7. Cooperation between Myo10 and Dynein-Mediated Mechanisms

(A–E) Cortical microtubule (MT) behaviors requiring Myo10 or dynein in RPE-1 cells expressing GFP-EB3.

(A) Schematic classification of lateral (a) and end-on (b) MTs used to determine the percentage of MTs undergoing lateral sliding (% Transition). All of the cortical astral MTs reaching a 1 μm cortical band are classified into lateral (red) or end-on (blue) based on the their displacement and orientation relative to the cell edge (see Figure S7A; Supplemental Information for details).

(B) Western blotting showing depletion of Myo10 and LGN protein by siRNA.

(C) Immunofluorescence images showing decreased cortical dynein and p150 localization after LGN RNAi (left), with corresponding fluorescence quantitation (right, n = 20 line scans from ten cells per condition, ***p < 0.0001, and non-parametric Student's t test). Note that in RPE-1 cells, LGN knockdown leads to significantly reduced cortical dynein or $p150^{Glued}$ during anaphase, unlike HeLa cells, where it has a more modest effect, due to parallel 4.1G/R-dependent cortical dynein recruitment (Kiyomitsu and Cheeseman, 2013).

(D) Overlay images of lateral (red) and end-on (blue) MTs from GFP-EB3 movies in indicated conditions (Movie S5) (right, without the overlay). The yellow indicates the MT trajectory prior to entry into the cortical band, whereas the blue/red correspond to trajectories within the cortical region classified as in (A). The outlines of the cell edge in the first and last frame (solid and dashed green lines) of the movie are shown. The scale bar represents 10 μm.

(E) Quantitation showing decreased lateral transitions after LGN knockdown (n = >100 spindles poles, each of which had ~2,500–4,000 MTs, per condition from four experiments, permutation t test, and ***p < 0.0003).

(F and G) Additive defects in spindle orientation (F) and centrosome clustering (G) after combinatorial inhibition of Myo10 and cortical dynein.

(legend continued on next page)

detectably alter subcortical actin structures, indicates that Myo10 is an important mediator of actin's effect on microtubule dynamics. The abrogation of this effect by point mutations in the Myo10 microtubule-binding domain (Figures 6D and S6C) strongly suggests a direct mechanism.

The analytical tools that we developed have enabled us to acquire the first in depth, large-scale analysis of cortical microtubule interactions in human cells (Figures 6, 7A–7E, and S7) and to uncover distinct, but overlapping, roles for Myo10 and dynein. Prior to anaphase, Myo10 plays an important role in mediating end-on microtubule cortical interactions (Figure 6E). Once cells enter anaphase, Myo10 becomes less important, with the microtubule motor dynein playing the dominant role in promoting lateral sliding of microtubules along the cortex (Figures 7D, 7E, and S7D). This is consistent with dynein's role in spindle positioning in other systems (Adames and Cooper, 2000; Pearson and Bloom, 2004). The absence of a dynein effect on lateral sliding during metaphase may be explained by the known antagonism of dynein by MAP4 during this stage of mitosis (Samora et al., 2011).

Together, our data demonstrate that Myo10 and dynein are the major motors that position centrosomes and spindles in somatic mammalian cells and that they largely act in parallel. This conclusion is supported by the following evidence. First, Myo10's role in spindle positioning requires its direct microtubule-binding capacity (Figures 3, S3, 6D, 6E, and S6C). Second, the localization of LGN or dynein is independent of Myo10 and vice versa (Figures 7C, S7G, and S7H). Third, Myo10 and dynein inhibition have distinct effects on microtubule dynamics and microtubule-cortical interactions (Figures 6, S6, 7D, 7E, and S7D). Finally, combined inhibition of Myo10 and dynein results in an additive defect in centrosome positioning (Figures 7F and 7G).

The mechanisms that underlie spindle orientation in human cells, as defined in the present study, have interesting parallels to spindle positioning mechanisms previously described in budding yeast (Adames and Cooper, 2000; Pearson and Bloom, 2004). The Bim1-Kar9-myosin V mechanism in yeast promotes end-on cortical-microtubule attachment, whereas the dynein mechanism promotes lateral sliding. Similar to what we now demonstrate for Myo10 and dynein in mammalian cells, the actin-dependent mechanism in yeast is dominant prior to anaphase, whereas dynein dominates during anaphase. Myo10, therefore, appears to have amalgamated functions for centrosome positioning accomplished by Bim1, Kar9, and myosin V in budding yeast. Thus, evolutionarily divergent cell types have reached convergent solutions to integrate the actin and microtubule cytoskeletons for centrosome and spindle positioning.

Unlike yeast, spindle positioning in animal cells is heavily influenced by the tissue microenvironment through cell matrix attachments and the position of retraction fibers (McCaffrey and Macara, 2011; Morin and Bellaïche, 2011; Théry and Bornens, 2006). Abnormalities in cell-matrix adhesion and tissue rigidity are commonly observed in disease states such as cancer (McCaffrey and Macara, 2011; Pease and Tirnauer, 2011). The current work defines the major motors required for centrosome and spindle positioning in human cells and provides a foundation for future work on this process in the context of development or disease.

EXPERIMENTAL PROCEDURES

Detailed descriptions of cell lines, culture conditions, plasmid construction, immunofluorescence microscopy, live-cell imaging, quantitation, automated image analysis, statistical analysis of the data, and antibodies used in this study can be found in the Supplemental Information.

Quantitation of Paxillin

Cells plated on FN-H patterns for 6 hr were fixed and stained for paxillin, phalloidin actin, and DNA. For measurements of focal adhesion area and total fluorescence intensity, paxillin images were subjected to background subtraction by the same image after Gaussian blur and discrete paxillin-positive structures were obtained across all conditions. There were two rectangular regions (75 × 255 pixels) along the adhesive surface of a FN-H pattern that were used for paxillin quantitation: images were applied for threshold and the subsequent objects selected were quantified using the "analyze particles" function in Image J software. Data presentation for histograms was done using Origin (Origin Lab).

Cell Division on Patterned Substrates

Cells were trypsinized, seeded on CYTOO chips, and assembled to the CYTOO chamber according to the manufacturer's instructions (CYTOO) 6–8 hr prior to fixation or live imaging. In some experiments, 20 μM of MG132 (Calbiochem) was used to enrich mitotic cells before fixation. For live imaging, the cell division plane was determined by the long axis of elongating anaphase cells at the time frame with the first appearance of a cleavage furrow and was measured using NIS elements software (Nikon Instruments). The angular distribution of spindle orientation was displayed using Origin (OriginLab).

Quantitation of Mitotic Cell Rounding

RPE-1 cells expressing RFP-H2B were plated on FN-L micropatterns and imaged at 10 min intervals by differential interference contrast (DIC) and fluorescence imaging. For the kinetics of mitotic cell rounding and post-mitotic cell spreading (re-adhesion), cell surface areas were measured using NIS elements software (Nikon Instruments) at the indicated time points.

Quantitation of Subcortical Actin Clouds and Spindle Pole Movements

HeLa cells expressing GFP-Utr-CH and mCherry-tubulin were imaged at a single confocal plane where both poles are visible (mid-cortical plane) at 15 s intervals for 15 min using a 60× objective (see Supplemental Information for details). To quantify subcortical actin clouds and spindle pole movements, kymographs were generated from a 70 pixel-width line along the major axis of the spindle. Cells in metaphase, as judged by chromosome configuration from DIC images, were analyzed. The penetration depth of the actin clouds into cytoplasm and their integrated fluorescence intensity were measured, as described (Fink et al., 2011). To quantify spindle pole movements relative to the actin cloud position (Figure S5A), the time intervals corresponding to each peak of GFP-Utr-CH were determined by line scans along the y axis of the kymographs. Pole velocity was obtained by quantifying the average slope of spindle pole position (both poles, determined by mCherry-tubulin signal) at each time interval (relative to the peak GFP-Utr-CH signal) using MetaMorph software.

(F) Imaging of U2OS cells on FN-L patterns and analysis as in Figure 1C. The right graph shows a Gaussian curve that was fitted to the data for each treatment shown in the left panel.

(G) The percentage of multipolar divisions in U2OS cells with extra centrosomes that express GFP-H2B for the indicated RNAi treatments. Approximately 70% of the cells have extra centrosomes after the transient overexpression of Plk4, as confirmed by centrin staining or spindle multipolarity that was induced by HSET RNAi (Kwon et al., 2008) (mean ± SEM). See also Figure S7.

Statistical Methods

To determine the significance of differences between conditions, a Student's t test (GraphPad Software) was used, unless otherwise specified. For Figure 2E, a one-way ANOVA and Tukey's multiple comparison tests were used to compare mean differences for all pairs. For all microtubule dynamics measurements, a permutation test was used to calculate statistical significance of changes in either the mean (when calculated per cell) or median (when pooled for multiple cells) of the distribution between conditions (see Supplemental Information for details).

Automated EB3 Comet Detection, Tracking, and Analysis of Astral EB3 Trajectories

The EB3 fluorescent comets were detected and tracked using a modified version of the plusTipTracker package (Applegate et al., 2011; Matov et al., 2010). Modifications were made to the watershed detection scheme in order to accommodate the large variance in fluorescence intensities observed in EB3-GFP mitotic cells and new methods for post-processing of the resulting EB3 trajectories were developed. Previously unpublished analytic schemes include the K-means clustering analysis, the cortical dwell time analysis, and the automated end-on versus lateral classifications. A discussion of the detection modifications, a listing of all detection/tracking parameters employed, and details regarding all newly developed EB3 trajectory analyses are provided in the Supplemental Information. All EB3 comet analyses were implemented in MATLAB (MathWorks).

SUPPLEMENTAL INFORMATION

Supplemental Information includes Supplemental Experimental Procedures, seven figures, and five movies and can be found with this article online at http://dx.doi.org/10.1016/j.devcel.2015.06.013.

ACKNOWLEDGMENTS

We thank M. Thery, B. Akins, H. Arellano-Santoyo, S. Jhaveri-Schneider, and N. Umbreit for comments on the manuscript; L. Ding for sharing computer code; the Nikon Imaging Center at Harvard Medical School and H. Elliott from the Image and Data Analysis Core at Harvard Medical School for their help with kymograph analysis of microtubule dynamics; and R. Cheney, W. Krek, E. Nigg, I. Cheeseman, T. Wittmann, and W. Bement for reagents. D.P. was supported by the Howard Hughes Medical Institute and the NIH (GM061345); M.K. was supported by a special fellow award from the Leukemia and Lymphoma Society and a Susan Komen grant; and M.B. and G.D. were funded by the NIH (GM067230).

Received: April 18, 2014
Revised: April 8, 2015
Accepted: June 12, 2015
Published: July 30, 2015

REFERENCES

Adames, N.R., and Cooper, J.A. (2000). Microtubule interactions with the cell cortex causing nuclear movements in Saccharomyces cerevisiae. J. Cell Biol. *149*, 863–874.

Applegate, K.T., Besson, S., Matov, A., Bagonis, M.H., Jaqaman, K., and Danuser, G. (2011). plusTipTracker: Quantitative image analysis software for the measurement of microtubule dynamics. J. Struct. Biol. *176*, 168–184.

Chang, F., and Martin, S.G. (2009). Shaping fission yeast with microtubules. Cold Spring Harb. Perspect. Biol. *1*, a001347.

Ezratty, E.J., Partridge, M.A., and Gundersen, G.G. (2005). Microtubule-induced focal adhesion disassembly is mediated by dynamin and focal adhesion kinase. Nat. Cell Biol. *7*, 581–590.

Fink, J., Carpi, N., Betz, T., Bétard, A., Chebah, M., Azioune, A., Bornens, M., Sykes, C., Fetler, L., Cuvelier, D., and Piel, M. (2011). External forces control mitotic spindle positioning. Nat. Cell Biol. *13*, 771–778.

Goshima, G., and Scholey, J.M. (2010). Control of mitotic spindle length. Annu. Rev. Cell Dev. Biol. *26*, 21–57.

Gusnowski, E.M., and Srayko, M. (2011). Visualization of dynein-dependent microtubule gliding at the cell cortex: implications for spindle positioning. J. Cell Biol. *194*, 377–386.

Hirano, Y., Hatano, T., Takahashi, A., Toriyama, M., Inagaki, N., and Hakoshima, T. (2011). Structural basis of cargo recognition by the myosin-X MyTH4-FERM domain. EMBO J. *30*, 2734–2747.

Honnappa, S., Gouveia, S.M., Weisbrich, A., Damberger, F.F., Bhavesh, N.S., Jawhari, H., Grigoriev, I., van Rijssel, F.J., Buey, R.M., Lawera, A., et al. (2009). An EB1-binding motif acts as a microtubule tip localization signal. Cell *138*, 366–376.

Kerber, M.L., and Cheney, R.E. (2011). Myosin-X: a MyTH-FERM myosin at the tips of filopodia. J. Cell Sci. *124*, 3733–3741.

Kerber, M.L., Jacobs, D.T., Campagnola, L., Dunn, B.D., Yin, T., Sousa, A.D., Quintero, O.A., and Cheney, R.E. (2009). A novel form of motility in filopodia revealed by imaging myosin-X at the single-molecule level. Curr. Biol. *19*, 967–973.

Kiyomitsu, T., and Cheeseman, I.M. (2012). Chromosome- and spindle-pole-derived signals generate an intrinsic code for spindle position and orientation. Nat. Cell Biol. *14*, 311–317.

Kiyomitsu, T., and Cheeseman, I.M. (2013). Cortical dynein and asymmetric membrane elongation coordinately position the spindle in anaphase. Cell *154*, 391–402.

Kleylein-Sohn, J., Westendorf, J., Le Clech, M., Habedanck, R., Stierhof, Y.D., and Nigg, E.A. (2007). Plk4-induced centriole biogenesis in human cells. Dev. Cell *13*, 190–202.

Kunda, P., and Baum, B. (2009). The actin cytoskeleton in spindle assembly and positioning. Trends Cell Biol. *19*, 174–179.

Kwon, M., Godinho, S.A., Chandhok, N.S., Ganem, N.J., Azioune, A., Thery, M., and Pellman, D. (2008). Mechanisms to suppress multipolar divisions in cancer cells with extra centrosomes. Genes Dev. *22*, 2189–2203.

Laan, L., Husson, J., Munteanu, E.L., Kerssemakers, J.W., and Dogterom, M. (2008). Force-generation and dynamic instability of microtubule bundles. Proc. Natl. Acad. Sci. USA *105*, 8920–8925.

Laan, L., Pavin, N., Husson, J., Romet-Lemonne, G., van Duijn, M., López, M.P., Vale, R.D., Jülicher, F., Reck-Peterson, S.L., and Dogterom, M. (2012). Cortical dynein controls microtubule dynamics to generate pulling forces that position microtubule asters. Cell *148*, 502–514.

Liu, R., Woolner, S., Johndrow, J.E., Metzger, D., Flores, A., and Parkhurst, S.M. (2008). Sisyphus, the Drosophila myosin XV homolog, traffics within filopodia transporting key sensory and adhesion cargos. Development *135*, 53–63.

Liu, K.C., Jacobs, D.T., Dunn, B.D., Fanning, A.S., and Cheney, R.E. (2012). Myosin-X functions in polarized epithelial cells. Mol. Biol. Cell *23*, 1675–1687.

Matov, A., Applegate, K., Kumar, P., Thoma, C., Krek, W., Danuser, G., and Wittmann, T. (2010). Analysis of microtubule dynamic instability using a plus-end growth marker. Nat. Methods *7*, 761–768.

McCaffrey, L.M., and Macara, I.G. (2011). Epithelial organization, cell polarity and tumorigenesis. Trends Cell Biol. *21*, 727–735.

McNally, F.J. (2013). Mechanisms of spindle positioning. J. Cell Biol. *200*, 131–140.

Minc, N., Burgess, D., and Chang, F. (2011). Influence of cell geometry on division-plane positioning. Cell *144*, 414–426.

Mitchison, T.J. (1992). Actin based motility on retraction fibers in mitotic PtK2 cells. Cell Motil. Cytoskeleton *22*, 135–151.

Mitsushima, M., Aoki, K., Ebisuya, M., Matsumura, S., Yamamoto, T., Matsuda, M., Toyoshima, F., and Nishida, E. (2010). Revolving movement of a dynamic cluster of actin filaments during mitosis. J. Cell Biol. *191*, 453–462.

Morin, X., and Bellaïche, Y. (2011). Mitotic spindle orientation in asymmetric and symmetric cell divisions during animal development. Dev. Cell *21*, 102–119.

Nagy, S., and Rock, R.S. (2010). Structured post-IQ domain governs selectivity of myosin X for fascin-actin bundles. J. Biol. Chem. *285*, 26608–26617.

Nagy, S., Ricca, B.L., Norstrom, M.F., Courson, D.S., Brawley, C.M., Smithback, P.A., and Rock, R.S. (2008). A myosin motor that selects bundled actin for motility. Proc. Natl. Acad. Sci. USA *105*, 9616–9620.

Pearson, C.G., and Bloom, K. (2004). Dynamic microtubules lead the way for spindle positioning. Nat. Rev. Mol. Cell Biol. *5*, 481–492.

Pease, J.C., and Tirnauer, J.S. (2011). Mitotic spindle misorientation in cancer—out of alignment and into the fire. J. Cell Sci. *124*, 1007–1016.

Pollard, T.D., and Borisy, G.G. (2003). Cellular motility driven by assembly and disassembly of actin filaments. Cell *112*, 453–465.

Redemann, S., Pecreaux, J., Goehring, N.W., Khairy, K., Stelzer, E.H., Hyman, A.A., and Howard, J. (2010). Membrane invaginations reveal cortical sites that pull on mitotic spindles in one-cell C. elegans embryos. PLoS ONE *5*, e12301.

Rodionov, V.I., and Borisy, G.G. (1998). Self-centering in cytoplasmic fragments of melanophores. Mol. Biol. Cell *9*, 1613–1615.

Rosenblatt, J., Cramer, L.P., Baum, B., and McGee, K.M. (2004). Myosin II-dependent cortical movement is required for centrosome separation and positioning during mitotic spindle assembly. Cell *117*, 361–372.

Samora, C.P., Mogessie, B., Conway, L., Ross, J.L., Straube, A., and McAinsh, A.D. (2011). MAP4 and CLASP1 operate as a safety mechanism to maintain a stable spindle position in mitosis. Nat. Cell Biol. *13*, 1040–1050.

Sandquist, J.C., Kita, A.M., and Bement, W.M. (2011). And the dead shall rise: actin and myosin return to the spindle. Dev. Cell *21*, 410–419.

Siller, K.H., and Doe, C.Q. (2009). Spindle orientation during asymmetric cell division. Nat. Cell Biol. *11*, 365–374.

Sun, Y., Sato, O., Ruhnow, F., Arsenault, M.E., Ikebe, M., and Goldman, Y.E. (2010). Single-molecule stepping and structural dynamics of myosin X. Nat. Struct. Mol. Biol. *17*, 485–491.

Théry, M., and Bornens, M. (2006). Cell shape and cell division. Curr. Opin. Cell Biol. *18*, 648–657.

Théry, M., Jiménez-Dalmaroni, A., Racine, V., Bornens, M., and Jülicher, F. (2007). Experimental and theoretical study of mitotic spindle orientation. Nature *447*, 493–496.

Toyoshima, F., and Nishida, E. (2007). Integrin-mediated adhesion orients the spindle parallel to the substratum in an EB1- and myosin X-dependent manner. EMBO J. *26*, 1487–1498.

Weber, K.L., Sokac, A.M., Berg, J.S., Cheney, R.E., and Bement, W.M. (2004). A microtubule-binding myosin required for nuclear anchoring and spindle assembly. Nature *431*, 325–329.

Wei, Z., Yan, J., Lu, Q., Pan, L., and Zhang, M. (2011). Cargo recognition mechanism of myosin X revealed by the structure of its tail MyTH4-FERM tandem in complex with the DCC P3 domain. Proc. Natl. Acad. Sci. USA *108*, 3572–3577.

Woolner, S., and Bement, W.M. (2009). Unconventional myosins acting unconventionally. Trends Cell Biol. *19*, 245–252.

Woolner, S., O'Brien, L.L., Wiese, C., and Bement, W.M. (2008). Myosin-10 and actin filaments are essential for mitotic spindle function. J. Cell Biol. *182*, 77–88.

Wu, L., Pan, L., Wei, Z., and Zhang, M. (2011). Structure of MyTH4-FERM domains in myosin VIIa tail bound to cargo. Science *331*, 757–760.

Yi, J., Wu, X., Chung, A.H., Chen, J.K., Kapoor, T.M., and Hammer, J.A. (2013). Centrosome repositioning in T cells is biphasic and driven by microtubule end-on capture-shrinkage. J. Cell Biol. *202*, 779–792.

Zhang, H., Berg, J.S., Li, Z., Wang, Y., Lång, P., Sousa, A.D., Bhaskar, A., Cheney, R.E., and Strömblad, S. (2004). Myosin-X provides a motor-based link between integrins and the cytoskeleton. Nat. Cell Biol. *6*, 523–531.

Zheng, Z., Wan, Q., Liu, J., Zhu, H., Chu, X., and Du, Q. (2013). Evidence for dynein and astral microtubule-mediated cortical release and transport of Gαi/LGN/NuMA complex in mitotic cells. Mol. Biol. Cell *24*, 901–913.

Developmental Cell

Supplemental Information

Direct Microtubule Binding by Myosin-10 Orients Centrosomes toward Retraction Fibers and Subcortical Actin Clouds

Mijung Kwon, Maria Bagonis, Gaudenz Danuser, and David Pellman

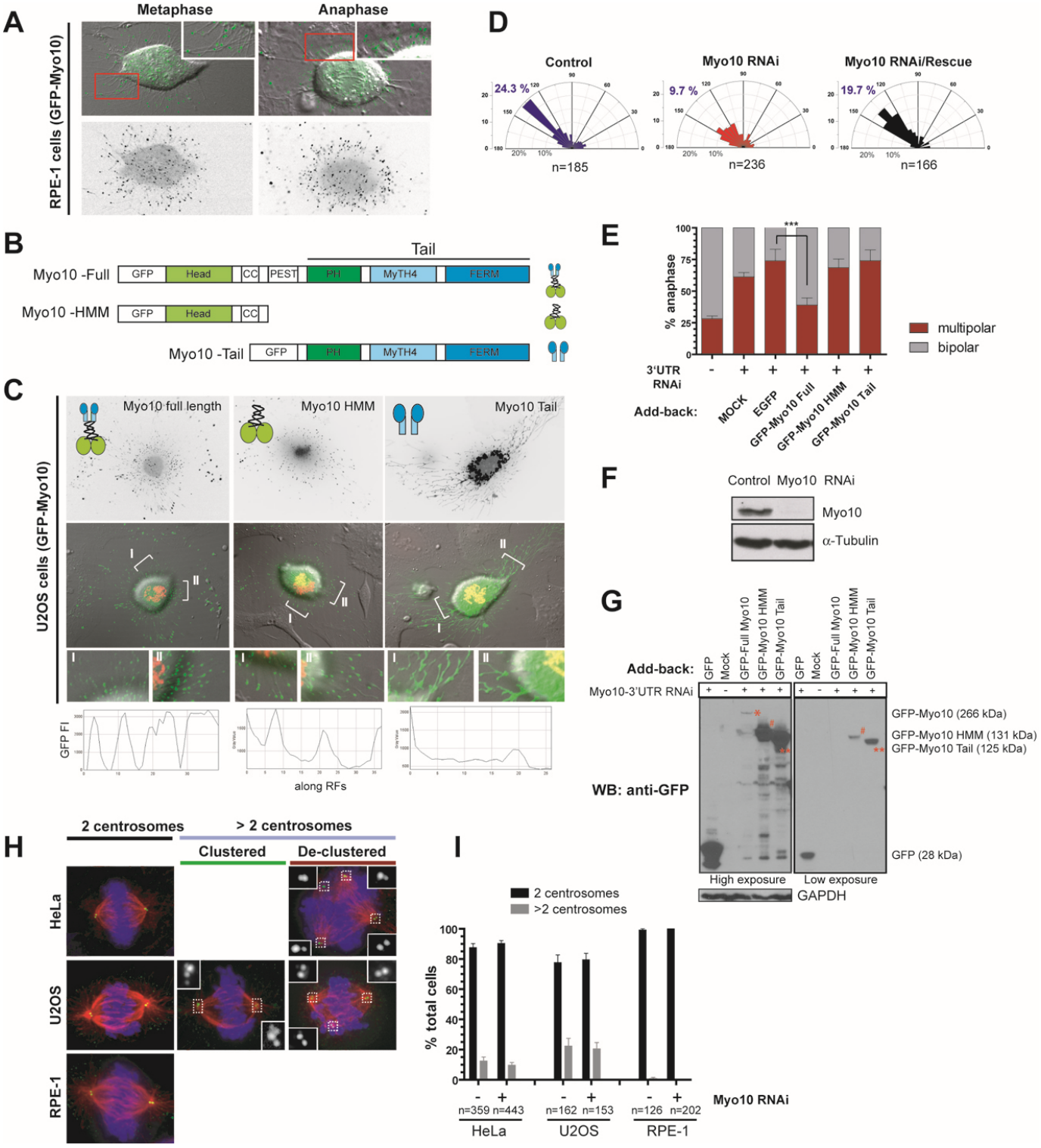

Figure S1 (related to Figure 1). The Motor Domain of Myo10 Is Sufficient for Retraction Fiber (RF) Localization; the Motor and Tail Domains Are both Required for Centrosome Positioning; Loss of Myo10 Does Not Induce Centrosome Fragmentation.

(A) Myo10 localizes to retraction fibers (RFs) during metaphase and anaphase in RPE-1 cells. GFP-Myo10 (bottom, inverted images) is overlaid on the DIC (RFs) images (insets, high magnification images of red box regions).

(B) Schematic of the Myo10 domain structure and of the GFP-tagged Myo10 constructs used for localization (C) and functional assays (E-G). Domains: Head, motor domain; CC, coiled coil; PEST, proline (P) glutamate (E) serine (S) and threonine (T) domain; PH, pleckstrin homology domain; MyTH4, myosin tail homology 4; FERM, four-point-one, ezrin, radixin, moesin domain.

(C) The motor domain, but not the tail domain, is required for localization of Myo10 to RFs. Images show U2OS cells expressing RFP-H2B and the indicated Myo10 constructs. Top panels: inverted images showing the GFP-Myo10 signal. Middle panels: merged images of DIC (RFs), GFP-Myo10 and RFP-H2B in mitotic cells. Bottom panels: high magnification images of RFs (in regions I and II) and the representative fluorescence line scans of GFP-Myo10 along RFs.

(D) Requirement of Myo10 for spindle orientation in U2OS cells expressing GFP-H2B on fibronectin (FN)-L patterns. Angular (α) distribution of the cell division axis in the indicated conditions (Fig 1C) was used to obtain the percentage of cells that were dividing with a median angle of 135 degrees ($\alpha = 135 \pm 10$) shown in Figure 1D.

(E) Both the motor and tail domains of Myo10 are required for complementation of centrosome clustering defects in cells depleted of endogenous Myo10. The percentage of anaphase cells with multipolar or bipolar divisions are shown in control cells (-) or cells depleted of endogenous Myo10 (+, 3'UTR RNAi) that were transfected with GFP (negative control) or the indicated Myo10 constructs. ***$p<0.002$, non-parametric Student's t-test. Data represents mean of 3 experiments ± s.e.m.

(F) Western blots showing the knockdown of Myo10 in U2OS cells.

(G) Western blots showing protein levels of rescue-incompetent Myo10 mutant constructs (Myo10 HMM and Tail) probed with anti-GFP antibodies. Blots with high (left) and low (right) exposure. *, GFP-Myo10; #, GFP-Myo10 HMM; **, GFP-Myo10 tail.

(H-I) Myo10 depletion does not affect centriole number or centrosome integrity in the cell lines used in this study.

(H) Representative immunofluorescence images showing centrin (green), α-tubulin (red), and DNA (Hoechst, blue). Insets: higher magnification of centrin images in boxed regions. Note that RPE-1 cells do not have extra centrosomes, and that HeLa cells cannot cluster extra centrosomes.

(I) Myo10 inhibition does not induce centrosome amplification in the cell lines used in the study. Note: We observed no centriole fragmentation, identified by a single centrin focus, nor spindle pole fragmentation, identified by ectopic spindle poles (α-tubulin-positive but without centrioles), after Myo10 depletion in any of the cell lines.

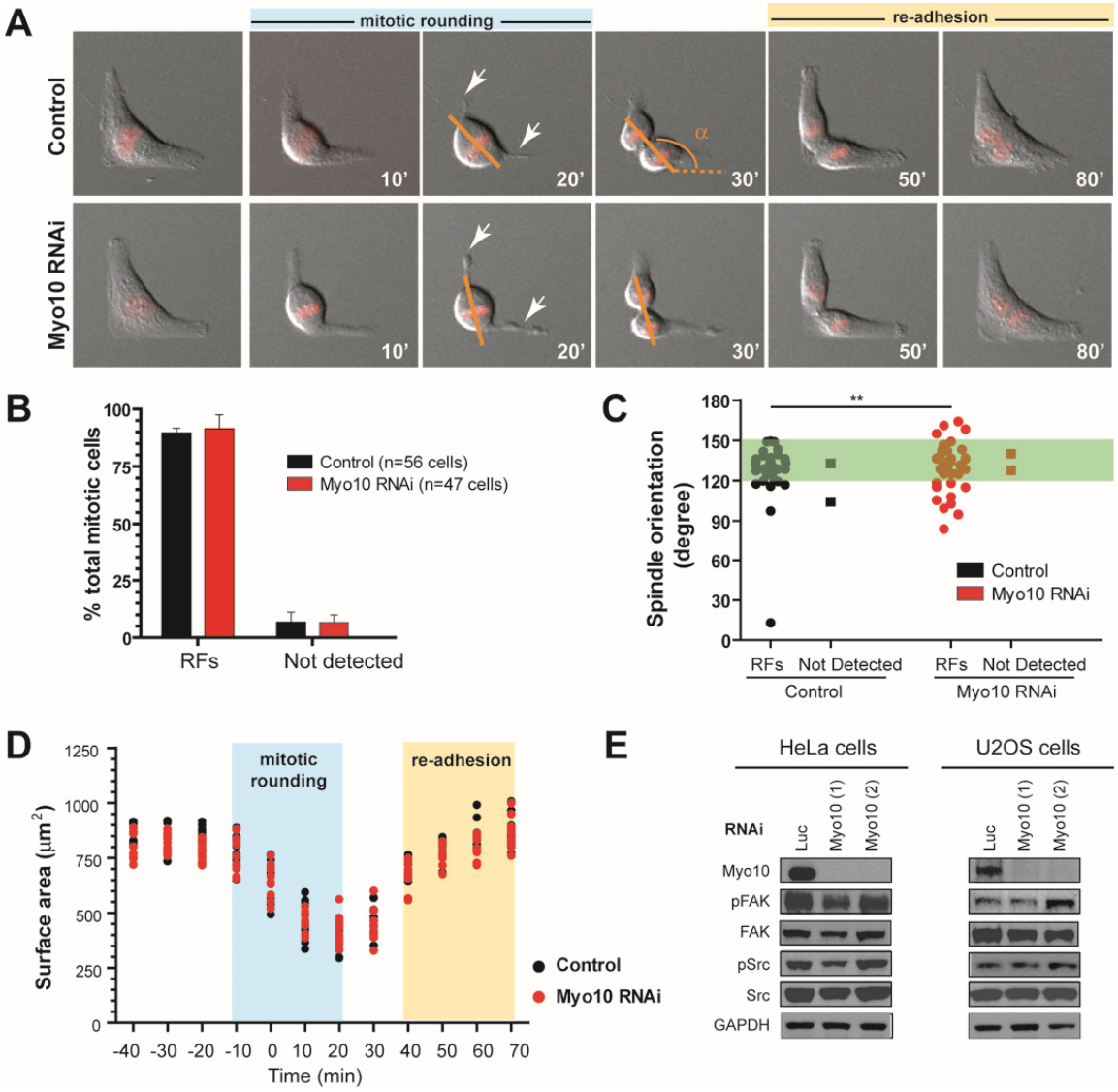

Figure S2 (related to Figure 2). Normal Retraction Fibers, Cell Adhesion and Mitotic Cell Rounding in Myo10-Depleted Cells despite Abnormal Spindle Orientation.

(A-D) Myo10-depleted RPE-1 cells exhibit well-defined retraction fiber (RF) regions and proper mitotic rounding, despite the presence of spindle orientation defects.

(A) Still images of live RPE-1 cells that express RFP-H2B dividing on FN-L patterns. Time: minutes from NEBD (t=0). Orange lines: cell division axis. Arrows: RF regions.

(B) Myo10 depletion does not affect the percentage of cells with RFs. Data represents mean of 3 experiments ± s.e.m. Note: ~ 4% of cells were not scored for each sample because the putative RF region was ambiguous or out of focus.

(C) Myo10-depleted cells with spindle orientation defects (outside of green area deviating from $120 < \alpha < 150$, **$p<0.05$, non-parametric Student's t-test, 2 experiments ± s.e.m) nevertheless have normal-appearing RFs. Quantitation of angular (α) distribution of cell division axis as in (A).

(D) No detectable defects in mitotic rounding and re-adhesion of Myo10-depleted cells. Mitotic cell rounding was quantified from live RPE-1 cells dividing on FN-L patterns as shown in (A). Each dot is an individual cell (n=10 cells per condition from 2 experiments).

(E) Western blots showing comparable levels of activation of FAK and Src in HeLa and U2OS cells depleted of Myo10 using two independent siRNAs. Luc: control siRNA.

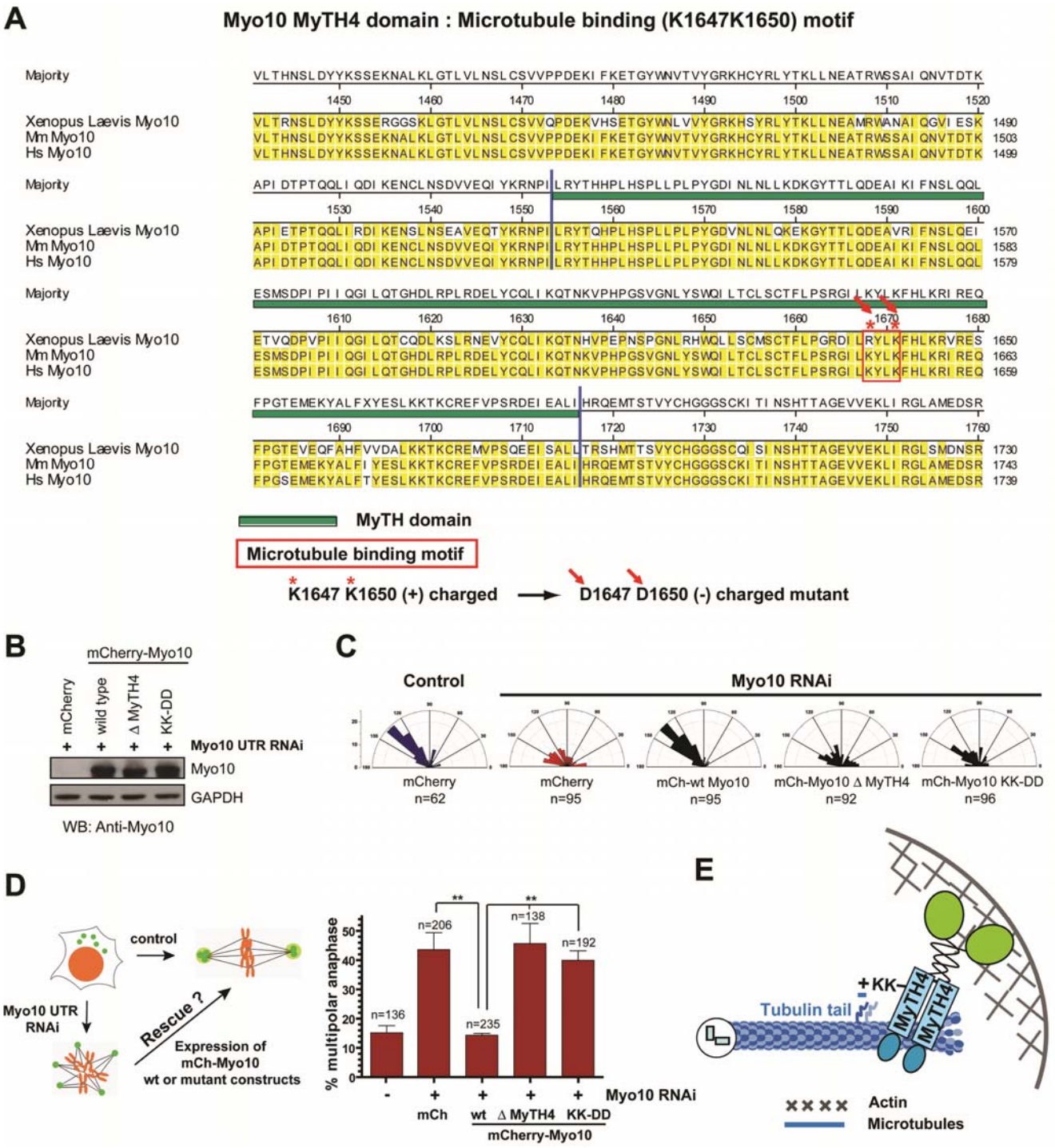

Figure S3 (related to Figure 3). Direct Binding of Myo10 to Microtubules Is Required for Centrosome Positioning during Mitosis.

(A) MyTH4 domain of Myo10 contains a microtubule binding motif. Amino acid sequences of *Xenopus*, Mouse (Mm), and Human (Hs) Myo10 were aligned by ClustalW; conserved residues are highlighted in yellow. MyTH4 microtubule binding domain (green bar) contains two positively (+) charged residues

(K1647/K1650) that have been shown to directly bind to tubulin tails [* in red box, (Hirano et al., 2011; Wei et al., 2011; Wu et al., 2011)].

(B) Comparable protein expression of mCherry-tagged Myo10 constructs used in siRNA-rescue experiments. Western blots were probed with anti-Myo10 antibodies.

(C) Requirement of Myo10 microtubule-binding for spindle orientation. Spindle orientation analysis was done as in Figures 1C-D for Figure 3C.

(D) Requirement of Myo10 microtubule-binding, but not its cargo-binding, for centrosome clustering. Left: Schematic of rescue experiment. Right: The percentage of multipolar or bipolar anaphases (GFP-H2B imaging) was scored in cells that expressed the indicated mCherry constructs (**$p<0.05$, non-parametric Student's t-test, 3 experiments ± s.e.m,). In this assay, ~ 12-14 h of doxycycline treatment led to ~ 85-90% of cells with extra centrosomes, as confirmed by centrin staining and spindle multipolarity induced by HSET RNAi (Kwon et al., 2008). Note: the modest difference in absolute numbers between results of this assay and that in Figure 7G is because in this experiment we used a longer time of Plk4 induction (See Supplemental Methods for details), which results in a higher initial frequency of cells with centrosome amplification; the experimental results shown in Figure 7G had ~ 70% of cells with extra centrosomes.

(E) Model: Electrostatic interaction between positively charged K1647/K1650 residues of Myo10 and negatively charged tubulin tail directly links microtubule lattice and actin to position centrosomes.

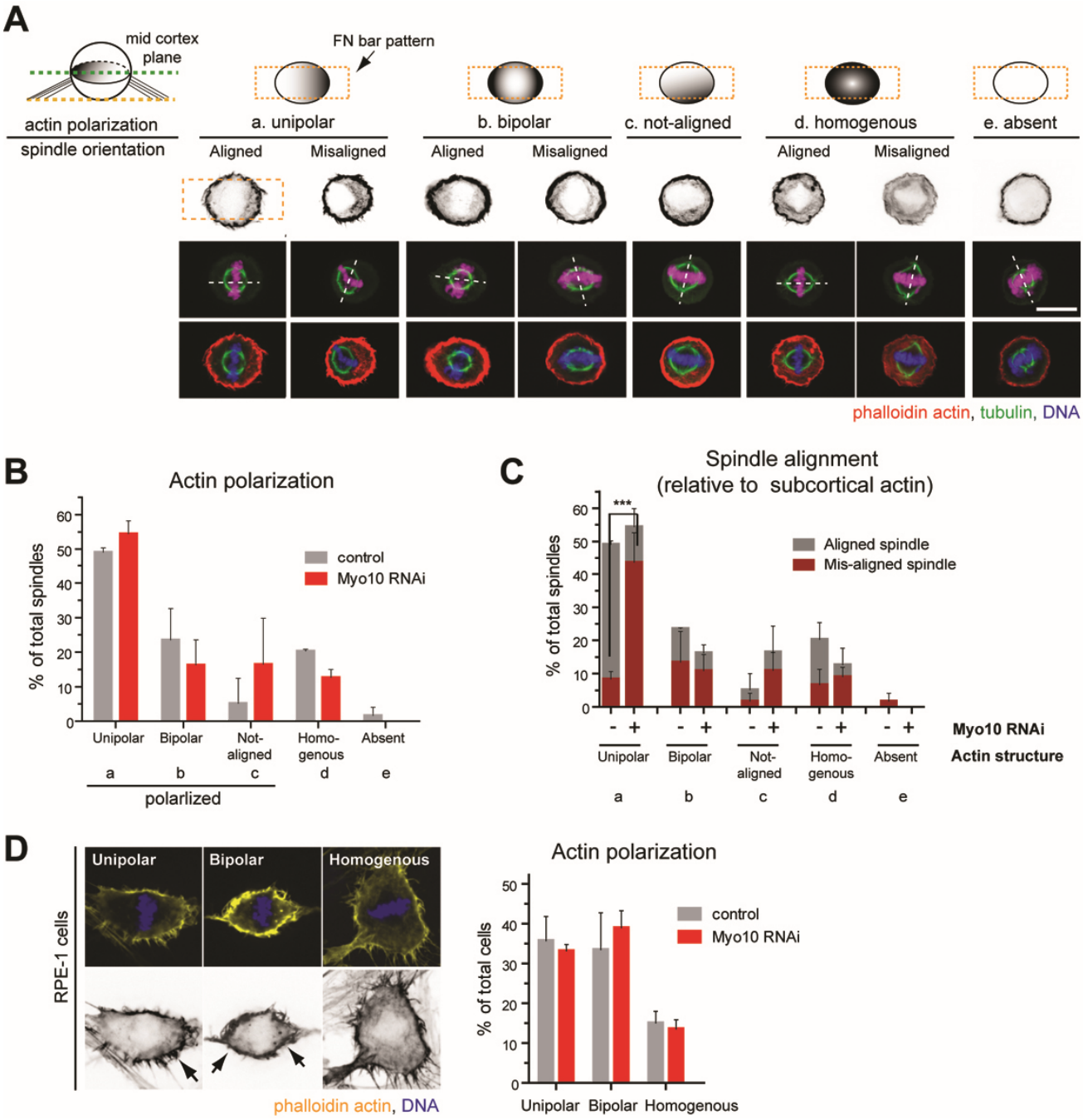

Figure S4 (related to Figure 4). Myo10 Is Required to Orient Spindles Relative to Subcortical Actin Clouds.

(A-C) Requirement of Myo10 for spindle orientation to the subcortical actin clouds in HeLa cells plated on FN-bar patterns.

(A) Characterization of the morphology of subcortical actin, including the rare categories where subcortical actin is asymmetric but not aligned with the pattern, and where subcortical actin is not detectable. Top: Schematic of the classification scheme used for subcortical actin polarity (Dark shade, subcortical actin concentration zone; yellow box area, adhesion surface of FN-bar patterns). Bottom: Representative

immunofluorescence images of HeLa cells quantified in (B-C). Cells were plated on bar patterns, fixed, and stained for phalloidin actin, tubulin, and DNA. The actin polarization pattern (inverted images) and spindle orientation axis (dotted white lines) are shown in the top and middle panels, respectively. Scale bar, 10 μm.

(B) Depletion of Myo10 has no significant effect on the positioning of subcortical actin relative to sites of adhesion. The percentage of metaphase cells that exhibit polarized (unipolar, bipolar, and not aligned relative to adhesion geometry), homogenous, or undetectable subcortical actin is shown for Myo10 RNAi and the control.

(C) Myo10 is required to orient spindles relative to unipolar subcortical actin clouds (***$p<0.001$, non-parametric Student's t-test, 3 experiments ± s.e.m).

(D) Depletion of Myo10 has no significant effect on the accumulation of subcortical actin clouds in RPE-1 cells. Left: Subcortical actin clouds in cells plated on FN-coated plates, and stained for phalloidin actin (yellow) and DNA (blue). Right: The percentage of metaphase cells that exhibit unipolar, bipolar, or homogenous subcortical actin is shown for Myo10 RNAi and the control.

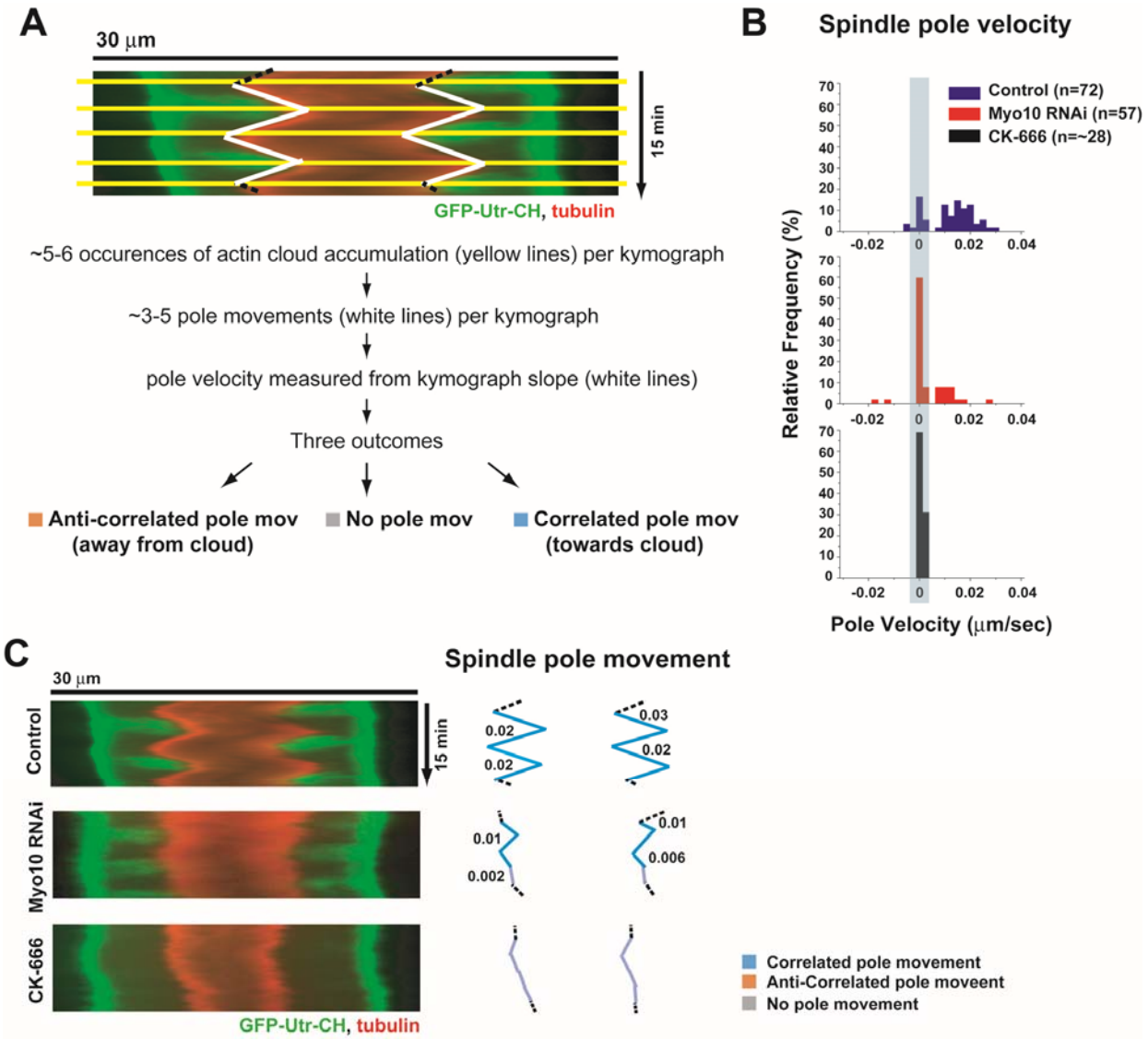

Figure S5 (related to Figure 5). Requirement of Myo10 for Actin Cloud-Mediated Pulling Forces on Centrosomes during Metaphase Spindle Oscillations.

(A) Schematic for the quantitation of actin cloud assembly dynamics and spindle pole movement relative to actin clouds shown in Figure 5B. Spindle pole movements relative to the regions of actin cloud accumulation were classified as correlated (blue, pole moves towards actin clouds), anti-correlated (orange, pole moves against actin clouds) or no (grey) movement. Significant pole movement was defined as a velocity that is more than 20% of the mean velocity measured in the control sample (mean=0.0125 μm/sec), based on the observed movements after Arp2/3 complex inhibition in (B).

(B) A decrease in spindle pole movements towards actin clouds in Myo10-depleted cells. Histogram of pole velocity toward (+) or against (-) actin clouds in indicated conditions (3 experiments). No movement (<0.0025 μm/sec, 20% of mean control value) is indicted by the grey box.

(C) Kymographs of actin clouds (green) and spindle pole (red) from the cells shown in Figures 5A-B in indicated conditions. Right: Representative traces of pole movements in kymographs (left) are color-coded according to the pole velocity classification in (A-B).

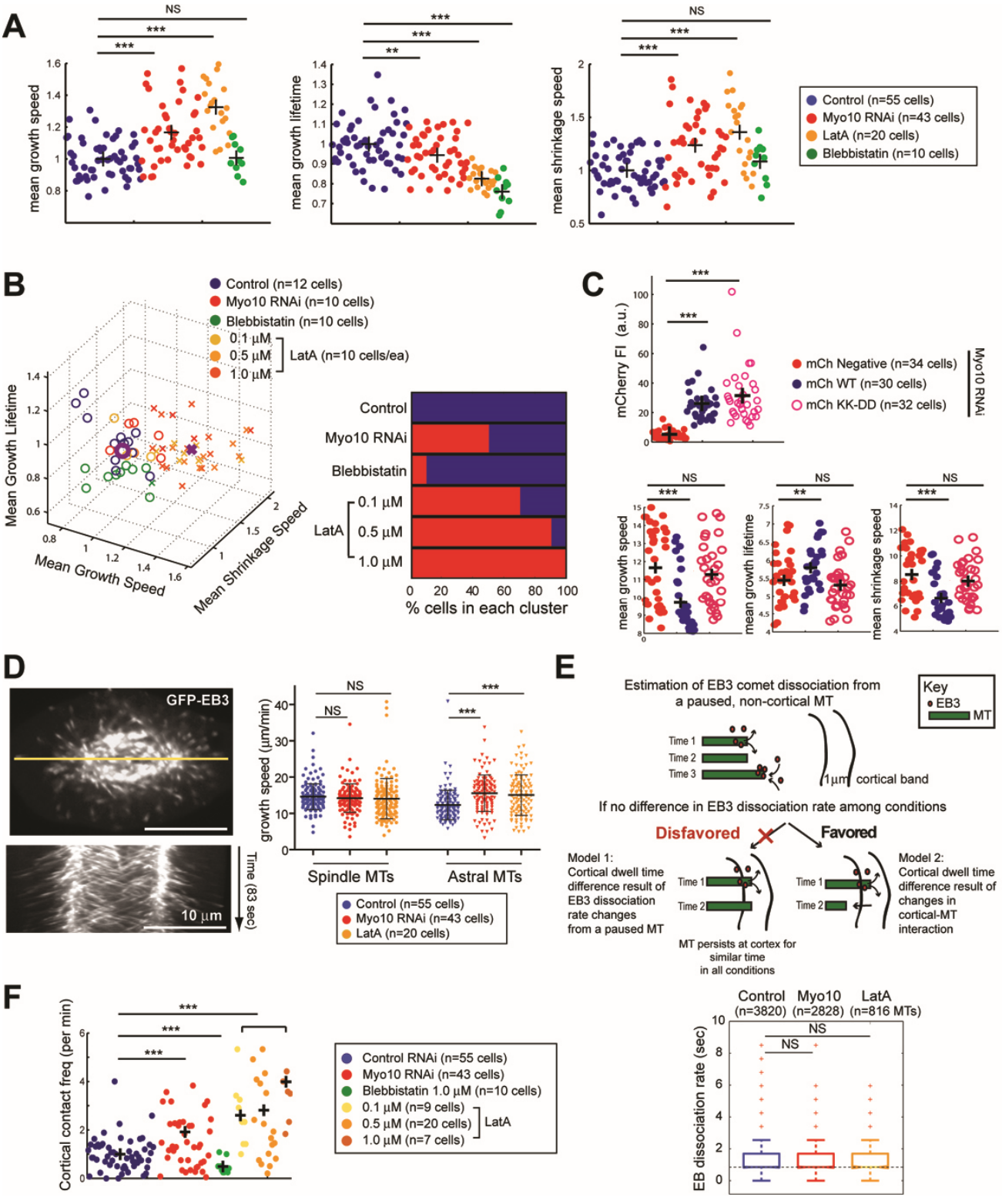

Figure S6 (related to Figure 6). Myo10 and Actin Suppress Cortical Microtubule Dynamicity Prior to Anaphase.

(A) Individual parameters of microtubule (MT) dynamics in control, Myo10-depleted, actin-disrupted (LatA treatment), or myosin II-inhibited (blebbistatin treatment) RPE-1 cells expressing GFP-EB3 (shown in Fig 6B). Each data point represents the average value for a given MT parameter from the entire astral MT population of each cell. The data are displayed as 2 dimensional (D) plots (unlike the 3D graph in Fig 6B) for visualization of differences between the samples for the individual parameters. Black crosses indicate the means for neighboring samples (Permutation test of the means, ***$p<0.0001$, **$p<0.02$).

(B) The effect of Myo10 on MT dynamics is distinct from a general disruption of cytoskeletal tension. Left: 3D plot of normalized mean MT growth speed, shrinkage speed, and growth lifetime, obtained from control cells (blue), cells depleted of Myo10 (red), or cells treated with blebbistatin (green) or different concentrations of LatA (different shade of yellow). Clustering of the data identified two distinct populations of cells that display highly (X) or less (O) dynamic MTs. Right: Unlike the effect of Myo10 knockdown, decreased myosin II-mediated contractility does not increase the percentage of cells with highly dynamic MTs (red). The relative percentages of cells that fall within the highly dynamic MT (red) or less dynamic MT (blue) category are shown for each condition.

(C) Requirement of Myo10 MT-binding for astral MT dynamics regulation. Top: Comparable expression (mCherry fluorescence intensity) of wild-type Myo10 or MT-binding (KK-DD) mutant used in the rescue experiment shown in Figure 6D (***$p<0.0001$, permutation test of the means, 2 experiments). Bottom: Individual parameters of MT dynamics are displayed as 2D plots (from the 3D graph in Fig 6D). Permutation test of the means, ***$p<0.0001$, **$p<0.05$.

(D) Myo10 depletion or actin disruption does not have a significant effect on MT growth speeds within the spindle. Left top: Single focal plane GFP-EB3 image of metaphase cell used for measurement of MT growth speed. Left bottom: Kymograph of the line generated along the long axis of spindle (horizontal and vertical scale bars represent 10 μm and 1.4 min). Right: MT growth speed within the spindle and astral MTs quantified from the kymographs in indicated conditions (***$p<0.0001$, non-parametric Student's t-test). Measurements sampled from the same 5 experiments shown in Fig 6B (error bars indicate s.e.m).

(E) The Myo10- or actin-dependent decrease in cortical dwell time is not the result of generally faster EB3 dissociation from the plus-ends of MTs. To determine whether Myo10 RNAi or LatA treatment affected EB3 dissociation from MT ends independent of cortical interaction, we measured the lifetime of EB3 on paused MTs outside the cortical region (see scheme and Supplemental Methods). The box plots show that the median EB3 dissociation rate is unchanged by Myo10 RNAi or LatA treatment (NS, permutation test of the medians, same 5 experiments shown in Figs 6B-C, E), which contrasts sharply with the data in Figure 6E where Myo10 RNAi or LatA treatment significantly affect EB3 comet cortical dwell time. Although there was no significant difference when the median values for Myo10 RNAi or LatA treatment are compared with the controls, there was a slight (~ 0.2 sec) but significant decrease in EB comet lifetime after Myo10 RNAi or LatA treatment when the mean values are compared ($p<0.01$ using a permutation test of the means). We attribute this difference to outlier measurements and a deviation from normality in these data (confirmed via Anderson-Darling tests) relative to the per cell data in Figures 6B, S6A, and S6F. This deviation makes the median value a potentially better descriptor of central tendency than the mean (See Supplemental Methods for details). Because Myo10 RNAi or LatA treatment has little or no effect on EB3 comet dissociation from paused MT plus ends, the EB3 cortical dwell time accurately reports MT-cortical interaction duration (Model 2).

(F) Increased contact frequencies of astral MTs with the cell cortex in LatA-treated or Myo10-depleted cells. Cortical contact frequencies were normalized by the mean of the control distribution acquired that day. The mean normalization value for the 5 pooled experiments was 17.8 ± 5.19 MT cortical tracks per min (***$p<0.0005$, permutation test of the means, 5 experiments).

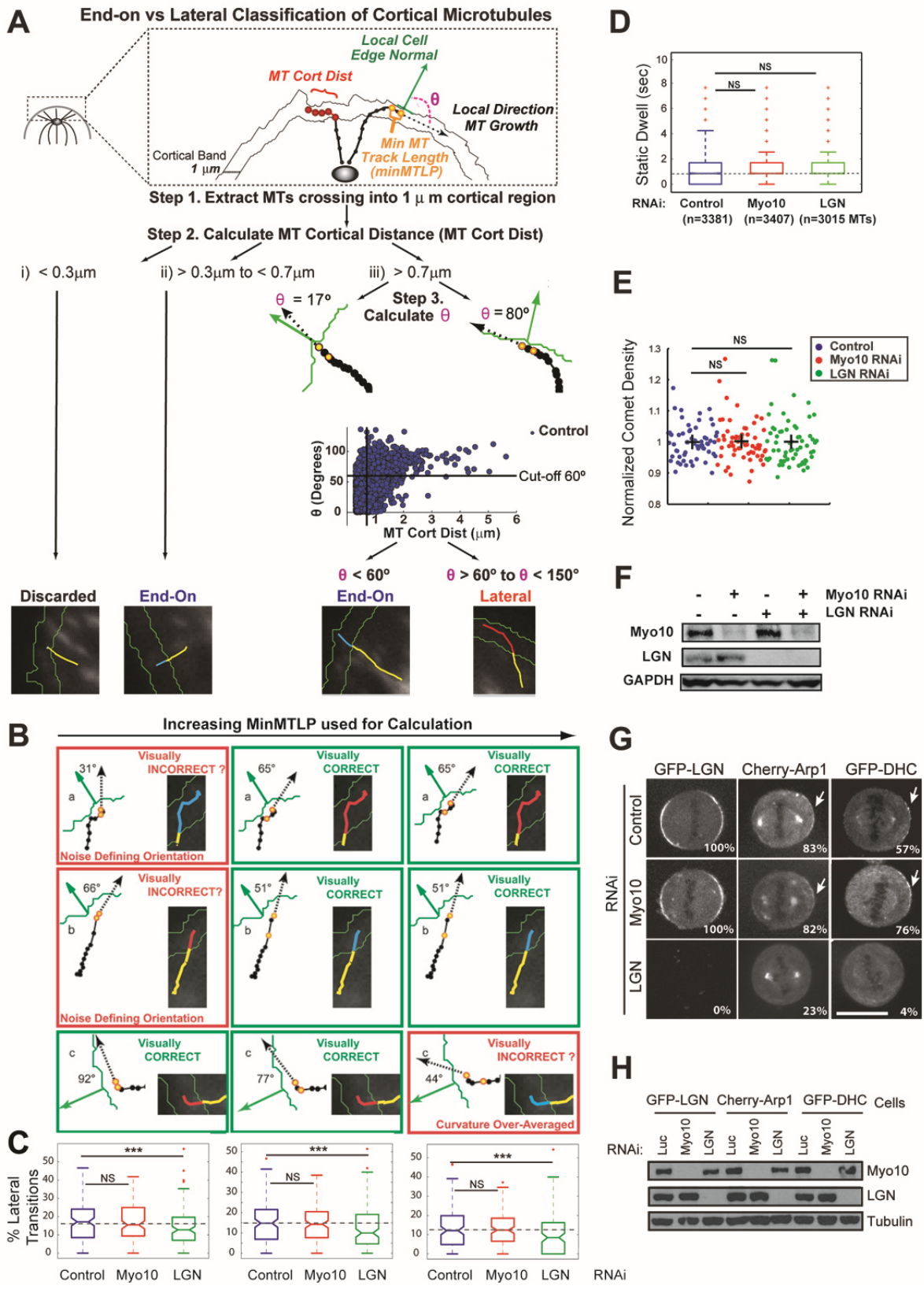

Figure S7 (related to Figure 7). Effect of LGN/Dynein in Mediating the Transition from End-on to Lateral Microtubules during Anaphase Is Robust, Specific, and Differs from That of Myo10.

(A) Scheme illustrating the automated algorithm to classify end-on and lateral cortical-microtubule (MT) capture. Note: The development of the algorithm necessitated implementing operational thresholds to distinguish the relevant categories of MT-cortical capture. However, we demonstrate that the conclusions are robust to small variation in the values for these thresholds (see below and the main text).

(Step 1) All astral MTs that crossed into the cortical band (1 μm from cell edge) were identified and analyzed.

(Step 2) The distance traveled by the MT within the cortical region (termed, MT Cort Dist) was measured, and initial MT classifications were made based on this parameter. If the MT traveled < 0.3 μm within the cortical band, the interaction was considered to be insignificant and was not analyzed further. MTs that traveled between 0.3 and 0.7 μm within the cortical band were considered to have significant cortical attachment. These interactions were considered to be end-on attachments by definition, because they fell below our threshold distance for lateral capture events. For MTs that traveled > 0.7 μm within the cortical band, we categorized lateral interactions based on the angle of movement relative to the cell edge.

(Step 3) To define the angle that MT ends move relative to the cell edge, we first identified the relevant track length for analysis, a parameter we termed the min MT Track Length parameter (minMTLP). The minimal track length that best discriminated lateral from end-on movement was defined empirically by matching the automated analysis to visual analysis. minMTLPs were then used to calculate the local direction of MT motion (dotted black vectors) relative to the direction perpendicular to the cell edge (termed the cell edge normal, green vectors). The resulting angle Θ (the MT orientation relative to the cell edge) was then calculated. Comet trajectories with Θs <60 degrees (blue) were classified as "end-on" attachment, whereas those that were 60< Θ <150 degrees (red), were classified as "lateral" attachments. The 60 degree cut-off for Θ was set because it was the minimum angle observed for MTs that traveled long distances (> 3 μm) within the 1 μm cortical band (see the graph of Θ versus MT Cort Dist).

(B-C) The conclusion that cortical dynein is required for the transition from end-on to lateral MT attachment is robust to modifications in the minMTLP threshold.

(B) We varied several parameters in the algorithm and found that the minMTLP had the most significant impact on our classification scheme (see Supplemental Methods). The minMTLP parameter determines the extent to which small displacements at the end of MT trajectories are considered to be significant. Three representative MT trajectories (named a, b, and c in the images) are shown, together with the classification that results when the minMTLP threshold is varied (216, 324, and 432 nm- left to right panels). Tracks are colored corresponding to their automated classification - end-on (blue) and lateral (red) - given the respective parameter settings. The specific MT track coordinates (minMTLP) used for calculation of the local MT orientation are highlighted as orange dots along the measured MT trajectory. MT classifications are boxed in green if marked "correct", or in red if marked "incorrect", by the experimentalist. The best correspondence between the automated analysis and manual curation of the data occurs with a minMTLP of 324 nm (middle panel). For MTs "a" and "b", a smaller (216 nm) minMTLP resulted in more experimentalist-defined cortical MT classification errors (Left panels); this is intuitive because the magnitude of the MT displacement determining the local MT growth direction (red/blue) vectors is closer to the measurement noise. A longer minMTLP (432 nm) can also result in experimentalist-called errors (Right panel, microtubule "c"); in this case, the longer minMTLP, which requires the use of longer portions of the MT trajectory for the calculation of the local MT growth direction, can result in over-averaging that may obscure the measurement of potentially significant MT track curvature.

(C) The effect of cortical dynein on lateral cortical MT interaction is robust and is apparent even when the minMTLP is varied. Shown are box plots of the percent end-on to lateral transitions, calculated using the

indicated minMTLPs (shown in B). Data were obtained with n >100 spindles poles per condition, from 4 experiments (Permutation test of the means, ***p<0.0003).

(D) Neither Myo10 nor cortical dynein significantly decreases the static dwell time of MTs during anaphase in RPE-1 cells. The box plots show that the median anaphase cortical dwell time is unchanged by Myo10 RNAi or LGN RNAi (NS by permutation test of the medians). A comparison of the mean values did reveal a small (~0.2 sec) but significant difference [(p< 0.001, permutation test of the means) (See Supplemental Methods for details)]. Note, this difference is not relevant to our conclusion, as it would suggest a slight increase in cortical dwell time, rather than a decrease. The difference between permutation tests of median and mean is related to some extreme outlier measurements in the distribution that make the mean value somewhat more variable in the re-sampling than the median.

(E) Depletion of Myo10 or LGN has no effect on the density of EB comets. A plot of EB comet density, normalized to the control, is presented (each data point: the average comet density from one cell).

(F) Western blots showing knockdown of Myo10, LGN, or both Myo10 and LGN by RNAi in the cells that are shown in Figure 7G.

(G-H) Cortical Dynein, Arp1 and LGN localization are not dependent on Myo10.

(G) Representative images showing that the localization of LGN, Arp1 and DHC as a lateral crescent (see arrows) at the cortex is unaffected by Myo10 RNAi (percentage of cells with polarized localization of cortical Dynein/LGN/Arp1 is indicated, ~50 cells per condition from 2 experiments). Shown are HeLa cells that express GFP-LGN, Cherry-Arp1 and GFP-DHC. The positive control (LGN RNAi) produces the expected defects in the recruitment of cortical LGN, Arp1 and DHC. Scale bar, 10 μm.

(H) Western blots showing efficient knockdown of Myo10 or LGN.

LEGENDS TO SUPPLEMENTAL MOVIES

Movie S1 (associated with Fig 1E): Forced tripolar division by retraction fiber (RF) mediated forces. Control GFP-H2B-expressing U2OS cells with extra centrosomes were plated on Y-shaped FN patterns and imaged. The movie illustrates that RF-mediated pulling forces decluster extra centrosomes, pull them towards the sites where RFs are anchored to the matrix (tips of the "Y"), resulting in tripolar cell division (Kwon et al., 2008). Extra centrosomes were induced by transient Plk4 overexpression (Kleylein-Sohn et al., 2007).

Movie S2 (associated with Fig 1E): Bipolar division or randomly oriented cell division after Myo10 RNAi in a GFP-H2B-expressing U2OS cell with extra centrosomes on Y-shaped FN patterns. This movie illustrates that Myo10 is required to couple forces originating from RF regions to astral microtubules (MTs) that position centrosomes.

Movie S3 (associated with Fig 5A): Comparison of spindle pole movement relative to subcortical actin clouds in control, Myo10-depleted or CK-666 (Arp 2/3 complex inhibitor)-treated HeLa cells expressing GFP-Utr-CH and Cherry-tubulin. Three movies (control, Myo10-depleted and CK-666-treated cells) are concatenated into a single movie.

Control (time=00:00:03): Spindle pole movement towards subcortical actin clouds, after a short time lag, in control cells. This movie illustrates retraction fiber and actin cloud-mediated pulling forces on centrosomes during spindle oscillations.

Myo10 RNAi (time=00:00:11): Decreased spindle movement towards subcortical actin clouds after Myo10 RNAi. This movie illustrates that Myo10 is not required for assembly or dynamics of actin clouds, but is required for pulling forces from actin clouds to position centrosomes.

CK-666 treatment (time=00:00:19): Decreased spindle movement after CK-666 (Arp 2/3 complex inhibitor) treatment. This movie illustrates the requirement of actin clouds for centrosome positioning.

Movie S4 (associated with Fig 6A-ii): Growth and inferred shrinkage events of microtubules (MTs) analyzed with plusTipTracker. The movie shows an example of MT trajectories from a control GFP-EB3-expressing RPE-1 cell, illustrating how a microtubule shrinkage event (yellow dashed line) may be inferred from the linkage of two collinear EB comet trajectories (cyan solid lines). Top Panel: Raw images of GFP-EB3 detection (cyan crosses). Bottom Panel: EB3 comet detection (cyan crosses), plus trajectory overlays (cyan solid lines) of two collinear EB3 comet trajectories that were linked by the algorithm as having a high probability of belonging to the same microtubule. plusTipTracker follows the EB3 comets (crosses) along the trajectory during MT growth phase. Shown is an example where a catastrophe event followed by a rescue

event is inferred. Note in both panels the detection and tracking of the surrounding EB3 comets are not shown for clarity.

Movie S5 (associated with Fig 7D): The behavior of microtubules at the cortex in control, Myo10-depleted or LGN-depleted RPE-1 cells expressing GFP-EB3. Three movies have been concatenated.

Control (time=00:00:00): Two distinct modes of astral microtubule (MT) interaction with the cell cortex during anaphase. Left Panel: Using automated classification (Fig S7A and Supplemental Methods), all astral MT trajectories crossing into the 1 μm cortical band (white overlays) are classified as end-on (blue) and lateral (red) cortical interactions; crosses mark the detected comet as it progresses along its MT track. The initial MT tracks, prior to entry into the cortical band, are plotted in yellow. Examples of high displacement MT trajectories (> 1.5 μm) that start and end within the cortical band (red dashed lines) as well as MT trajectories that cross into the cortical band but traveling < 0.3 μm within the cortical region (white), are shown here for completeness, although they were excluded from the formal analysis. Only high confidence MT trajectories (> 5 frames) are plotted. Right Panel: Raw images, including red arrow overlays that point to specific lateral MT transition events within the cortical band, as defined by our automated classification. All classifications were made using a Minimum Track Length parameter of 3 pixels (~300 nm, see Fig S7A).

Myo10 RNAi (time=00:00:24): Myo10 depletion does not affect the frequency of lateral cortical MT attachment during anaphase.

LGN RNAi (time=00:00:46): Inhibition of cortical dynein by LGN RNAi impairs lateral cortical MT attachment during anaphase.

EXTENDED EXPERIMENTAL PROCEDURES

Cell Culture

All cell lines were maintained at 37^{o}C with 5% CO_2 atmosphere in DMEM (U2OS, HeLa, Utr-CH-GFP and tubulin-mCherry HeLa), DMEM:F12 (hTERT RPE-l), or DMEM:F12 medium without phenol red (H2B-mCherry RPE-1, EB3-GFP RPE-1), or DMEM medium without phenol red (H2B-GFP and H2B-mCherry U2OS, LGN-GFP HeLa, Apr1-mRFP HeLa, DHC-GFP HeLa). EB3-GFP RPE-1 cell line is a gift from W. Krek (Thoma et al., 2010). LGN-GFP HeLa, Arp1-mRFP HeLa, and DHC-GFP HeLa cell lines are gifts from I. Cheeseman (Kiyomitsu and Cheeseman, 2012). Media were supplemented with 10% FBS, 100 IU/ml penicillin and 100 μg/ml streptomycin. The tetracycline-inducible U2OS cell line expressing Plk4 [a gift from E. Nigg, (Kleylein-Sohn et al., 2007)] was grown in DMEM supplemented with 10% of tetracycline-

free FBS, 100 IU/ml penicillin and 100 μg/ml streptomycin, 50 μg/ml hygromycin and 100 μg/ml G418. Plk4 expression was induced by addition of 2 μg/ml doxycycline for ~8-14 h.

siRNA and Plasmid Transfection

RNAi experiments were conducted using the RNAi MAX transfection reagent (Invitrogen). Sequence information of the small interference RNA (siRNA) pools used from Dharmacon are as follows: human Myo10 set of 4 ON-TARGETplus MYO10 siRNA L-007217-00-0002, (J-007227-08) 5'-GGAGGAAAUUUCAGGGAAU-3', (J-007217-07) 5'-GCGGGAGAAUUGUAGAUUA-3', (J-007217-06) 5'-CGUCGUAGCUGAUGUCUUA-3', (J-007217-05) 5'-GGACAUAAAUCUCAACUUG-3'; Human LGN/GPSM2 set of 4 ON-TARGETplus siRNA MU-004092-00-0002, (D-004092-01) 5'-GAACUAACAGCACGACUUA-3', (D-004092-02) 5'-GAGAAUGGAUGAACAGAGA-3', (D-004092-03) 5'-CAGAUUAGAUGAUCAAAGA-3', (D-004092-04) 5'-GGGCAAUGCUUAUUUCUAU-3'; human siGENOME Myo10-3'UTR siRNA D-007217-19-0005, 5'-CAACACUAAUCGACCGUAA-3'; human custom Myo10-5'UTR siRNA, 5'-UGGAGGAAGAAGAGACAAAUU-3'; human custom Myo10-5'UTR siRNA, 5'-UGAGGAACUUGGAGGAAGAUU-3'.

Plasmid transfection was carried out either using Lipofectamine 2000 (Invitrogen) for HeLa and U2OS cells or Neon Transfection System (Invitrogen) for RPE-1 cells, according to the manufacturer's protocol.

Drug Treatments

50 μM PF573228 (Tocris Bioscience), or 25 μM PP2 (Calbiochem), were added 2 h after cell spreading, and maintained in culture for 24 h. Nocodazole (Sigma) was added at 10 μM for 4 h to completely depolymerize microtubules (MTs) for focal adhesion disassembly assays, and at 100 ng/μl for 6 h for mitotic arrest. Latrunculin A (Invitrogen) was used at 0.1, 0.5, or 1 μM, Blebbistatin (Sigma) at 1 μM, and Arp2/3 complex inhibitor CK-666 (EMD Millipore) at 100 μM, prior to imaging. MG132 (Calbiochem) was used at 20 μM for 2-3 h.

Immunofluorescence Microscopy

Cells were plated on FN-coated coverslips or FN micro-patterned coverslips, as described (Kwon et al., 2008). For most experiments, to preserve Myo10, actin and retraction fiber morphology, cells were washed in pre-warmed PBS, and fixed in PBS containing 4% paraformaldehyde for 15 min at 37ºC, followed by permeabilization in PBS-0.5% Triton X-100 for 15 min. To visualize cortical dynein and p150, cells were washed with PBS, pre-extracted with PBS-0.2% Triton X-100 for 30 sec at room temperature, and fixed in cold methanol at -20ºC for 5 min. To visualize pFAK or centrin, cells were fixed in cold methanol at -20ºC,

rehydrated in PBS, and treated with PBS-0.25% Triton X-100 for 5 min. After permeabilization, cells were immersed in blocking buffer (PBS containing 5% BSA and 0.1% Triton X-100) for 40 min, and incubated with primary antibodies at room temperature for 1 h, washed with PBS-0.1% Triton X-100 and incubated with fluorescence-conjugated secondary antibodies (1:1,000, Molecular Probes) or/and Alexa Fluor Phalloidin (1:250, Molecular Probes) at room temperature for 1 h. Cells were also stained for DNA with Hoechst 33342 (1:5,000, Invitrogen) in PBS and coverslips were mounted with ProLong Antifade mounting medium (Molecular Probes).

Images were acquired either by a Yokogawa CSU-22 spinning disk confocal mounted on a Zeiss Axiovert microscope (Zeiss) or by a Yokogawa CSU-X22 spinning disk confocal with Spectral Applied Research Borealis modification on a Nikon Ti inverted microscope (Nikon Instruments). A series of 0.5 μm optical sections were acquired using x60 or x100 objective lens with an Orca ER CCD camera (Hamamatsu Photonics). Acquisition parameters, shutters, filter positions and focus were controlled by Slidebook software (Intelligent Imaging Innovations) or by MetaMorph 7 software (Molecular Devices).

Antibodies for Immunofluorescence

Samples were incubated with primary anti-rabbit centrin2 (1:200, Santa Cruz), anti-rabbit pFAK (Y-397, 1:200, Invitrogen), anti-rabbit Myo10 (1:300, Novus Biologicals), anti-rabbit DHC (1:100, Santa Cruz Biotech. Inc), anti-mouse p150 (1:200, BD Transduction Laboratories), anti-mouse Paxillin (1:200, BD Transduction Laboratories), anti-mouse monoclonal α-tubulin (DM1a, 1:500, Sigma), and anti-mouse monoclonal α-tubulin (clone B-5-1-2, 1:3000, Sigma) antibodies.

Cell Adhesion Assay

For the kinetics of FAK and Src activation, cells were trypsinized and replated on FN-coated plates [10 ng/μl as described, (Kwon et al., 2008)] to allow cell attachment. To avoid disturbing integrin-mediated adhesion signaling, cells were lysed directly in dishes while attached, at 1, 5, 18 h post-attachment.

Focal adhesion assays were performed as described (Ezratty et al., 2005). Briefly, serum-starved cells were grown on FN-coated coverslips, treated with 10 μM nocodazole for 4 h to completely depolymerize MTs, washed with warm PBS three times, and released to regular medium for 1 h to allow MT repolymerization.

Long Term Live-cell Imaging

Cells grown on glass-bottomed 12-well tissue culture dishes (Mattek) or in CYTOO chamber (CYTOO) were imaged on a Nikon Ti-E inverted microscope equipped with a precision motorized stage (Bioprecision, Ludl), and the Nikon Perfect Focus system enclosed within a temperature- and CO_2-controlled environment that

maintained an atmosphere of 37°C and 5% humidified CO_2. Images were captured at multiple points every 10 min for 2-3 days with a x20 objective and a cooled CCD camera (Coolsnap HQ2, Photometrics) controlled with NIS elements software (Nikon Instruments Inc.). Captured images from each experiment were analyzed using NIS-Elements software.

Immunoblotting

Immunoblotting was carried out as described (Kwon et al., 2008). Samples were incubated with the primary antibodies: anti-rabbit FAK (1:4000, Cell Signaling), anti-rabbit pFAK (Y-397, 1:5000, Invitrogen), anti-rabbit pSrc (Tyr416, 1:1000, Cell Signaling), anti-rabbit Src (1:1000, Cell Signaling), anti-rabbit Myo10 (1:2000, Novus Biologicals), anti-rabbit Myo10 (1:5000, Sigma), anti-rabbit LGN (1:2000, Bethyl Laboratories, Inc.), anti-rabbit KIFC1 (1:1000, Proteintech), anti-rabbit mCherry (1:500, BioVison), anti-mouse GAPDH (1:240000, Ambion), anti-mouse GFP (1:12000, Roche Applied Science), and anti-mouse monoclonal α-tubulin (DM1a, 1:15000, Sigma).

Plasmid Construction and Gene Replacement Experiments

To generate N-terminal mCherry-tagged Myo10 constructs (mCherry-Myo10-pLenti-CMV-Puro), siRNA resistant versions of mCherry-Myo10 constructs were synthesized. The C-terminal 2.8 kb of Myo10 for wild type or 2.8 kb of KK-DD mutant or 2.2 kb of ΔMyTH4 mutant were synthesized into pUC57-Amp (AgeI/HindIII) and the internal BglII site was removed by site-directed mutagenesis (Agilent Technologies). The N-terminal 3.4kb of wild-type Myo10 was subcloned into pUC57-Amp using BglII/AgeI upstream of the C-terminal fragments; the subsequent full length wild-type Myo10 or Myo10 KK-DD (6.2kb) or Myo10 ΔMyTH4 (5.6 kb) constructs were subcloned into pENTR mCherry C2, using BglII/ HindIII. These constructs were transferred to pLenti- CMV-Puro DEST (Addgene#17452) via an LR clonase reaction. High titer lentivirus was prepared by concentrating the virus using PEG-it virus precipitation solution (System Biosciences), and was used to infect U2OS cells expressing GFP-H2B and Plk4 under the control of a tetracycline-inducible promoter.

For the centrosome clustering assays, U2OS cells expressing doxycycline (Dox)-inducible Plk4 (Kleylein-Sohn et al., 2007) were used to induce extra centrosomes; their clustering efficiency was assessed by scoring bipolar or multipolar divisions. U2OS cells expressing GFP-H2B or mCherry-H2B were subjected to two consecutive Myo10 3' UTR RNAi or to Myo10 ORF RNAi (J-007227-05, J-007227-06, J-007227-08) treatments, in order to deplete the endogenous protein. A double thymidine block was performed, as described (Kwiatkowski et al., 2010): thymidine for 18-20 h, release for 8-10 h with doxycycline induction of Plk4 during this time, then a second thymidine block, followed by release. For each experiment, the population of cells harboring extra centrosomes was assessed by two independent methods,

immunofluorescence microscopy to quantify centriole numbers, and live imaging of cells depleted of HSET to quantify spindle multipolarity induced by HSET RNAi (Kwon et al., 2008). In U2OS cells, HSET inhibition induces multipolarity in proportion to the fraction of cells with extra centrosomes.

For the knockdown-add-back rescue experiments (Fig S1B-G) to determine the effects of Myo10 constructs on centrosome clustering, cells expressing RFP-H2B were transfected with wild-type or mutant Myo10-GFP plasmids [gifts of R. Cheney, (Cox et al., 2002)] during the first thymidine release for additional 4 h (total of 12-14 h doxycycline induction), and 24 h prior to imaging. For lentiviral infection (Fig S3D), cells expressing GFP-H2B were infected with lentivirus containing wild-type or mutant Myo10- mCherry, as described above (total of 12-14 h doxycycline induction). For the rescue experiments of spindle orientation on FN-L patterns (Fig 3B), double thymidine block and lentivirus infection were performed, as described above without doxycycline treatment. Only cells that were positive for GFP-Myo10 or mCherry-Myo10 at comparable expression levels were subjected to quantitation, as gauged by the fluorescence intensity of Myo10 (NIS elements software). For measurements of mCherry-rescue protein expression level, the mean fluorescence intensity of mCherry was quantified from 20x20 pixel-square regions of cells.

Live Imaging of Subcortical Actin Clouds and Spindle Pole Movements

HeLa cells were transfected with GFP-Utr-CH [a gift from W. Bement, (Woolner et al., 2008)] and GFP-positive cells were selected by fluorescence-activated cell sorting (FACS). FACS sorted cell clones were screened microscopically for optimal expression and visualization of actin clouds. These GFP-Utr-CH-expressing clones were then infected with an adenovirus containing mCherry-tubulin (gift of T. Wittmann) for 4 h. The double positive cells expressing GFP-Utr-CH and mCherry-tubulin were used for imaging within 7 days, a time interval during which mCherry-tubulin expression remains optimal. Cells were plated on 35 mm glass-bottomed tissue culture dishes (Mattek) and images were acquired at a single confocal plane where both poles are visible (mid-cortical plane) at 15 s intervals for 15 min using a x60 objective without binning.

High Resolution Live Cell Imaging for Microtubule Dynamics

Clonal RPE-1 cells that stably express GFP-EB3 were plated on 35 mm FN-coated glass-bottomed tissue culture dishes (Mattek) and imaged at 37^{o}C in DMEM-F12 phenol red free medium containing 10% FBS (Invitrogen).

To obtain images with high spatio-temporal resolution suitable for automated EB comet tracking and the extraction of parameters describing microtubule (MT) dynamics, cells were imaged at a single confocal plane for DIC and GFP. All images were collected with a Yokogawa CSU-X1 spinning disk confocal head with Spectral Applied Research Borealis modification on a Nikon Ti inverted microscope equipped with x60 Plan Apo NA 1.4 objective lens and Perfect Focus System. The microscope was enclosed in a custom-built

incubator at 37 °C and with 5% CO_2. EGFP-EB3 fluorescence was excited with a 491nm solid state laser controlled with an ATOF, and emission was collected with a Semrock 405/491/561/642 multipass dichroic mirror and a Chroma 525/50 ET emission filter. Images were acquired every 0.75 sec for 100 time frames without binning, using a Hamamatsu ORCA ER cooled CCD camera controlled with MetaMorph 7 software (Molecular Devices).

Cells were imaged in the optical plane of horizontally positioned spindles, with both poles visible at the mid-cortex (i.e. corresponding to the position of subcortical actin clouds). Cell cycle stage for metaphase and post-anaphase cells were determined by the chromosome configuration from DIC images. To visualize lateral MTs in post-anaphase cells (Figs 7A-E, S7A-C) with similar pole-to-cortex distances (3-5 μm), cells were treated with 100 ng/μl of nocodazole for 6h, released to pre-warmed medium, and imaged during the 30-90 min window after release.

Statistical Methods for MT Dynamics and MT-cortex Interaction Measurements

For all MT dynamics measurements (Figs 6B-D, S6A-C, S6F, S7E), we characterized cell-to-cell variability in the MT dynamics (for 7E, S7C, the data was analyzed per spindle pole). In Figures 6B, S6A-B, and S6F, to eliminate unavoidable systematic variation between daily experimental set-ups, each per cell MT dynamic value was normalized by the mean of the control cellular distribution for a given MT parameter obtained that day. Similarly, in Figure 6D, per cell MT values were normalized to the mean of the mCherry-WT cellular distribution. This normalization maintained consistency between Figures 6B and 6D, facilitating cross-comparison. For these cellular distributions, permutation tests were used to calculate statistical significance of changes in the mean between all conditions. Note, while a permutation test for differences in the means was always employed, as this test requires no assumptions regarding normality, this test will provide near identical results to a student's t-test if the dataset distribution does approach normality, which was typically the case for our per cell distributions.

In contrast, statistics related to cortical static dwell (Figs 6E, S7D) and the measurements of the EB3 dissociation rate from paused, non-cortical MTs (Fig S6E) were performed on pooled data from multiple cells. This was because the sample size that could be obtained per cell was limited (Sampled N in metaphase was 1-50 MTs per cell for the control condition). The data from these pooled samples deviated from normality to a greater extent than the per cell distributions (confirmed via Anderson-Darling tests), and contained some outliers, making the median value a potentially better descriptor of central tendency than the mean (see Legends to Figs S6E and S7D). A slight skew from outliers with long dwell times is in fact expected, given that longer dwell times are easier to measure than shorter dwell times with 0.85 second interval image acquisition. Therefore, the permutation test was used to calculate statistical significance of changes in the median between conditions in these cases. For all statistical comparisons related to the MT dynamics

parameter data the number of permutations for each permutation test was calculated based on sample size: maximum permutations = 10000 for very large sample sizes.

For box plots shown in Figures 6E, S6E, 7C, 7E, S7C, and S7D, the middle bar of the box indicates the median value of population, while the top and bottom bars indicate the 75th (q3) and 25th (q1) percentiles of the population. The extension of the whiskers is calculated as $q_3 + 1.5(q_3 - q_1)$ and $q_1 - 1.5(q_3 - q_1)$, respectively. Data beyond the whiskers are shown as plus-signs (+) and may be considered as outliers to the distribution. However, in all our statistical tests, these values were included, as discussed above.

EB3 Comet Detection and Tracking

Settings for detection and tracking of EB3-GFP comets for all conditions are as follows. The EB3 fluorescent comets for analysis of all MT dynamics were detected and tracked with use of a modified version of the plusTipTracker package (Applegate et al., 2011; Matov et al., 2010). Images were filtered using a difference of Gaussians, band-pass filter (sigma1 = 1 pixel and sigma2 = 2 pixels) to dampen both high and low frequency noise in the image and facilitate comet detection. Given the high density of the comets in mitotic cells, we used the watershed method for their detection (Applegate et al., 2011). The high concentration of EB3 decorated MTs within the spindle resulted in a tendency for EB3 mitotic images to display higher intra-cellular variance in fluorescence intensity than that seen for interphase cell images on which the package was developed (Applegate et al., 2011). Therefore, in this study the standard deviation of the intracellular background was estimated by fitting the first mode of the filtered intensity signals to a Gaussian function. Detection accuracy was verified manually and cells with poor detection were excluded from the data set. However, once the above modifications were made, detection problems were rare.

MT tracking parameters were set to be consistent for all conditions. Frame-to-frame linking parameters were set to a minSearchRadius of 2 pixels (216 nm) and a maxSearchRadius of 5 pixels (540 nm). MT growth tracks with a track length of less than 3 frames were discarded from further analysis.

The plusTipTracker software was designed to perform frame-to-frame linking of EB3 comet detections, and also to infer undecorated MT pause, shrinkage and undetected growth events by associating collinear, sequential growth sub-tracks (i.e. EB3 comet trajectories), which likely belong to the same MT, into compound tracks via a global optimization scheme (Applegate et al., 2011; Matov et al., 2010). MT growth subtrack linking parameters (i.e., "gap closing" parameters) were set as follows; maxForwardAngle = 30 degrees, maxBackwardAngle = 10 degrees, fluctuation radius = 2 pixels (216 nm), maximum shrinkage factor =1.5, and maxGapLength = 12 frames (~10 secs). Forward subtrack linking was performed to both correct for occurrences wherein a comet might disappear temporally from the field of view, prematurely breaking the EB3 trajectory, as well as to identify MT pause events where the EB3 comet disassembles from the MT. These respective events can be identified based on the velocity of the gap linkage. Slow gap linkage

velocities more likely correspond to EB3 comet dissociation from the MT, whereas fast linkage velocities more likely correspond to EB3 bound MTs that leave the focal plane temporarily. Cut-offs for classifying fast forward subtrack linkages as undetected growth events were determined for each experimental day, and estimated via unimodal thresholding (Rosin, 2001) of the pooled forward gap speed distribution. Forward gap speeds above the threshold were considered undetected growth events, and interpolated MT growth coordinates were added to link the two MT growth subTracks. Forward gap speeds below the threshold were considered MT pause events, in which the EB3-comet dissociates from the MT due to an interruption in net MT polymerization, but does not exhibit measurable depolymerization (i.e. shrinkage). All backward subtrack linkages were classified as MT shrinkage events that were eventually 'rescued', transitioning back to EB3 associated MT regrowth at a spatial point along the first MT growth subtrack, behind the site of the original comet disappearance.

As documented previously (Applegate et al., 2011; Matov et al., 2010), one potential artifact in inferred shrinkage measurements corresponds to the false linking of very parallel moving MT tracks: mitotic cells tend to exhibit a higher number of very parallel MT tracks relative to interphase cells (for which the software was developed). Therefore, one may anticipate the frequency of backward links to increase when measuring shrinkage rates via plusTipTracker during mitosis. However, we expect that if the distributions corresponding to the local orientation of the candidate subtracks remained constant for all conditions tested, the probability of a linking artifact occurring would likewise remain constant, and thus not contribute to changes in the shrinkage rate observed among conditions. We measured the relative orientation of all pairs of candidate EB comet trajectories that fulfilled the backward linkage criteria and noted no statistically significant difference in this measurement among the perturbation conditions. We infer that the frequency of the artifact from parallel tracks was constant for all conditions tested, and therefore does not explain differences in shrinkage speed observed among the experimental conditions.

Measurements of Global Astral Microtubule Dynamics

As described above, all RPE-1 cells for this analysis were imaged in the optical plane of the equator of horizontally positioned spindles. Estimation of the cell-edge for the astral region of interest was obtained from intensity thresholding of the EB3 GFP channel by rosin-based thresholding (Rosin, 2001). All masks were assessed visually for accuracy. Cells for which a visually acceptable mask could not be obtained via automated intensity thresholding were discarded from the analysis. In cases of significant cell-edge movement, the cell-edge masks were updated in each frame. These cell edge measurements were used in all cortical MT analyses requiring a cell edge estimate.

Non-astral (i.e. mitotic spindle) regions were delineated manually, and were subtracted from the whole cell region of interest, to obtain an astral specific mask. For each mitotic cell, all tracked astral MTs

were extracted using the plusTipSubRoiExtractTracks function in plusTipTracker. Only those EB3-decorated MT trajectories that exhibited at least 50 percent of their total lifetime within the astral region were included in the analysis; only those portions of the astral EB3 comet trajectories that fell within the astral region were used to calculate the lifetime and speed of the EB3-decorated MT trajectory; and only those shrinkage events that displayed 100 percent of their inferred coordinates within the astral subregion were included in the analysis.

To more directly monitor cell-to-cell heterogeneity following a given perturbation condition, we calculated the mean value for each of the MT parameters (EB3 comet speed, inferred MT shrinkage speed, and EB3 comet lifetime) for the astral MT distribution measured for each cell (~750 EB3 comet decorated MT trajectories and ~ 90 shrinkage events measured per cell). Because we observed subtle but significant fluctuations in the MT dynamics parameters of control cells from one experimental day to another, likely due to slight and unavoidable changes in the experimental conditions, we normalized the data to its respective daily experimental control population before pooling the data from different experimental days. For each experimental day corresponding to the RNAi or LatA treatment experiments (Fig 6B), the average of the per cell MT measurements for the control cells was calculated, and all per cell MT dynamics measurements for that day were divided by this value, such that all control normalized values scattered around a value of 1. In the case of the Myo10 depletion-add-back experiments (Figs 6D, S6C), a similar normalization procedure was employed using the values corresponding to the mCh-Myo10-WT (wild-type) add-back condition. This normalization allows a direct comparison of all add-back experiments with the data presented in Figures 6B-C and 6E (left panel).

Measurement of Per Cell Expression Level of Rescue Constructs

To obtain a per cell estimate of Myo10 construct expression level in the MT dynamics rescue experiments, an automated procedure was developed where cell edge masks, obtained in the EB3 fluorescence channel, were used to collect the mean intra-cellular, background-subtracted fluorescence intensity in the mCherry channel. Extra-cellular background in mCherry signal was estimated per-frame by averaging the mCherry fluorescence intensity values in the extracellular region as defined from the cell edge mask. The background estimate was subtracted on a pixel-by-pixel basis from the raw intensity values. Negative pixel intensity values upon background subtraction were set to zero.

Clustering Cells with Similar Astral Microtubule Dynamics

Calculations of the normalized mean for each MT parameter (EB3 comet speed, inferred MT shrinkage speed, and EB3 comet lifetime) per cell were collected for 5 experimental days (three days when cells were treated with control or Myo10 RNAi; two days when cells were treated with control or Myo10 RNAi, or with 0.5

μM LatA), and were plotted in 3-dimensions, to assess whether cells that exhibit changes in one parameter (such EB3 comet speed) likewise exhibit large stereotypical changes in the other two MT dynamics parameters (Fig 6B). The kmeans clustering function in Matlab R2012b (20 replicates, all other parameter set to default) was used to identify two groups of cells that exhibited similar MT dynamics behavior: the identities of cells in each cluster were obtained, and we calculated the percentage of cells from a given experimental treatment in each of the two MT dynamics clusters (Figs 6C-D, S6B). A permutation test of the means was likewise used to confirm the statistical significance of the difference between control and perturbation conditions for each of the three measured MT dynamics parameters (Figs S6A, S6C, EB3 decorated MT growth speed, inferred MT shrinkage speed, and EB3 decorated MT growth lifetime).

Cortical Region Creation and Microtubule Trajectory Extraction

We used the bwdist function in Matlab 2012b to create a cortical region that was 1.0 μm from the cell edge, and extracted all measured EB3 bound microtubule (MT) trajectories that crossed into this cortical region from the non-cortical astral region of the cell (Figs 6E, 7A, S7A). MT trajectories were defined as those tracking measurements corresponding to an explicitly detected EB3-GFP comet (i.e. no inferred shrinkage or pausing behavior was considered in the cortical analysis); we reasoned that this definition was most consistent with previous studies that employed manual MT EB3 comet tracking. Only measured MT growth trajectories crossing once into the cortical region were considered for cortical calculations in this study, as these tracks are unequivocally from a single MT**.** To be considered a viable trajectory for analysis, the cortical MT trajectory likewise had to persist for more than 5 frames (3.4 sec).

Static Dwell Calculations

Cortical classifications were first performed as described below (See Classification of End-on vs. Lateral MT Cortical Interactions section of Supplemental Methods) to classify all EB3 comet decorated MT trajectories that cross into the cortical region into either end-on or lateral growing MTs. Only tracks classified as end-on were used for the calculations of static dwell: we reasoned that MT dwell at the end of a laterally growing track likely represents a distinct molecular event. To calculate the time that the decorated MT was immobilized at the cortex, small masks with a diameter that was 2 pixels (~216 nm) wide were made around the coordinate corresponding to each EB3 comet decorated trajectory endpoint (i.e. the point where the EB3 comet is no longer detected, either due to comet dissociation or due to the MT permanently leaving the focal plane of the image). The static dwell was calculated from the number of frames in which the EB3 comet centroid was detected within the respective local dwell mask (Fig 6E). Note that we excluded EB3 trajectory endpoint events where the EB3 signal disappeared and subsequently reappeared within the cortical band (See EB3 Comet Detection and Tracking section of Supplemental Methods for details regarding

detection/definition of these events). This is a distinct cortical event from EB3 decorated, MT persistence before catastrophe that we aimed to measure.

Measurements of Spindle Microtubule Growth

EB3 comet intensity is extremely dense within the spindle region and the associated MTs exhibit much more complex dynamic behavior than the interphase data on which plusTipTracker was originally tested. In addition, optimization of the imaging conditions for EB3 comet detection and tracking in the astral region, our primary region of interest, often required saturating the pixels in the image corresponding to the spindle. These factors prevented the application of plusTipTracker to generate reliable EB3 trajectories in this region. Hence to test for the regional specificity of the MT dynamic changes in the Myo10 RNAi or LatA treatment condition to the astral region, kymograph analysis was employed.

For Kymograph analysis, the same data set where astral MTs were analyzed by plusTipTracker (Figs 6B-C) was used to generate GFP-EB3 kymographs to obtain MT growth speeds in both the spindle region and for the astral MTs (Fig S6D). For each cell, a kymograph was generated from a 2-pixel wide line drawn along the major axis of the spindle, encompassing the entire length of the cell. MT growth speeds were calculated by measuring the slopes of GFP-EB comet trajectories, as previously described (Stumpff et al., 2012; Tirnauer et al., 2002). Spindle MTs growing towards the equator and astral MTs growing toward the cell periphery were analyzed to measure MT growth speeds in the spindle and astral regions, respectively. Data were presented as distributions of individual MT growth speeds pooled from multiple cells per condition. The same results were obtained when all measurements from a single cell (for spindle and astral regions) were averaged to obtain a mean MT growth speed per cell for each region, and their distributions were compared in different conditions. Note that the kymograph analysis orthogonally validates the alterations in astral MT dynamics detected by plusTipTracker after Myo10-knockdown or LatA-treatment.

Estimation of EB3 Dissociation Rate

We considered the possibility that the decreased cortical dwell time observed in Myo10 depleted or LatA-treated cells, as calculated via the EB3 marker, could be due solely to a faster dissociation rate of EB3 from the MT in these conditions (Fig S6E, Model 1), rather than reflecting a true decrease in the time the MT persists at the cortex before depolymerization (Fig S6E, Model 2). To test this possibility, we obtained an estimate for the global EB3 dissociation rate from a paused MT in different experimental conditions. To achieve this, MT pausing events that were accompanied by EB3 comet dissociation and followed by subsequent EB3-decorated MT regrowth were isolated using the plusTipTracker's 'gap closing' algorithm as described above (See EB3 Comet Detection and Tracking section of Supplemental Methods). These EB3 dissociation rate calculations were performed in precisely the same manner as the cortical dwell

measurements with the exception that, for cortical dwell measurements, only terminal EB3 trajectory endpoints or EB3 trajectory endpoints linked to a rescue event were considered (Fig S6E, upper panel). For EB3 dissociation rate analysis we considered the global population of paused MTs followed by regrowth assuming that effects of Myo10 depletion and LatA treatment on the kinetics of the comets would be the same throughout the cell.

Definition and Measurement of Mitotic Poles

For all anaphase cells, coordinates for the two centrosomes were documented manually from the first frame of each movie, using the impoint function in Matlab 2012b; these two coordinates were used to calculate the long axis of symmetry corresponding to the cell. A single line perpendicular to this long axis of symmetry, and passing through the cell center, was used to define the pole-specific cortical regions for the analysis of the percent lateral transition (Figs 7D-E). We used the coordinates corresponding to the intersection between the long axis of symmetry and the edge of the cell mask in the first frame to calculate the pole to cortex distance (d) with regard to each centrosome. As the pole-to-cortex distance is decreased, lateral MT events increased significantly; thus, all measurements of anaphase cortical MT parameters (Figs 7A-E) were obtained from spindle poles with a d of 3-5 μm for all conditions.

Classification of End-on vs. Lateral Microtubule Cortical Interactions

EB3-decorated microtubules (MTs) that travel short distances (MT Cort-Dist) within the cortical region (between 0.3 μm and 0.7 μm) were designated *a priori* as perpendicular ("end-on") MT events: we assumed that differences in orientation for these low-displacement tracks were likely due primarily to either noise or other factors that did not correspond to the more robust, potentially motor-driven, lateral sliding of interest [Fig S7A Step 2 (ii)]. EB3-decorated MTs traveling a distance (MT Cort-Dist) of less than 0.3 μm in the cortical region were discarded from further analysis: we reasoned that these tracks did not contain enough cortex-specific-information to make a robust MT classification [Fig S7A Step 2 (i)]. EB3-decorated MTs traveling a distance (MT Cort-Dist) greater than 0.7 μm within the cortical region were further filtered via their local orientation relative to the cell-edge, to assign them to either the lateral or perpendicular MT-cortical interaction class [Fig S7A Step 2 (iii)].

For each of the measured trajectories of MTs traveling a distance (MT Cort-Dist) > 0.7 μm within the 1 μm cortical band, we calculated the local direction of MT motion at the very end of the measured MT trajectory (Fig S7A, dotted black vector). The specific coordinates of the measured MT trajectory used for this vector calculation were dictated by the Minimum MT Track Length parameter [minMTLP, (Figs S7A-B)]. As an EB3-decorated MT very often pauses at the cortex before comet-loss/ MT depolymerization, EB3 comets may exhibit small displacement fluctuations in their direction of movement, simply due to the noise

in the measurement. To prevent these noise-driven directional changes from dominating the local direction of MT motion measurement, detected coordinates were iteratively scanned backward in time along the measured MT trajectory until the Euclidean distance between the EB3 coordinate under question and the terminal MT trajectory coordinate was greater than or equal to the minMTLP (Fig S7A-B). Coordinates along each measured MT trajectory that fulfilled this distance criterion were then used to calculate the respective local direction of MT motion in the cortical region. Note that the minMTLP used for the local direction of MT motion calculations should be large enough to average out small changes in MT direction due to noise, but should be small enough so to not dampen the measurement of true MT track curvature corresponding to the lateral transitions that exhibit lower subsequent displacement (Fig S7B). We found that a minMTLP of approximately 3 pixels (324 nm) falls roughly within this category, as verified by manual classification of tracks by an experimentalist (Fig S7B, middle panels).

Once the direction of local MT motion was established for each MT, this value was used to calculate the orientation of movement of each cortical MT relative to the cell edge (Fig S7A step3). To make this calculation, we had to measure the local orientation of the cell edge: to this end, we found the point along the cell edge that was closest to the terminal coordinate of each MT trajectory. Coordinates of the cell edge within a radius of 10 neighboring pixels (~1 μm) centered on this point were extracted, and designated as the local cell edge for each corresponding MT. From these edge coordinates, the normal to local cell edge (green vectors, the direction perpendicular to the cell edge) was calculated with use of the princomp function in Matlab 2012b**.**

Using the above two vectors, we calculated the orientation of the MT relative to the local cell-edge normal (Θ). Those MTs with a local direction of MT motion forming an angle > 60 degrees and < 150 degrees with respect to the local cell edge normal (i.e. EB3 comets traveling approximately perpendicular to the cell edge normal and thus moving parallel to the cell edge), were designated as lateral MT trajectories (red in plots), whereas those MTs with a local direction of MT motion forming an angle < 60 degrees with respect to the cell edge normal were designated as end-on MT trajectories (blue in plots). The value of 60 degrees was considered to be a reasonable cut-off for determining lateral transitions, as this was approximately the lowest orientation value exhibited by MTs that are traveling long distances within the 1 μm cortical region (see scatter plots of MT track orientation vs. MT cortical displacement in Fig S7A). This behavior was consistent for all perturbation conditions tested.

Test for Robustness of Conclusions to Small Changes in Parameters

We recognize that manual classifications are inherently subjective and that what constitutes a “correct”, biologically meaningful classification may slightly differ among individuals (Fig S7B). Therefore, while validation of the automated classifications against manual classifications is important, it is insufficient. The

power of a fully automated analysis lies in the fact that the criteria for classification can be standardized, and different definitions of a lateral MT interaction can be systemically explored. To this end, we varied the minimum MT track length used for the local MT orientation calculation, a parameter that dictates the degree to which small-displacement changes in the direction of MT motion at the very end of the measured MT trajectory are considered significant. (Figs S7A-B). We observed little change in the overall shape of the orientation vs. displacement distribution (scatter plots in Fig S7A) for the different choices of minimum MT track length parameter (minMTLP); based on this result, a cut-off of 60 degrees for the MT orientation relative to the cell edge was considered reasonable in all cases. As anticipated, increasing the minMTLP used to calculate the local MT orientation relative to the cell edge tended to decrease the absolute value of the percent lateral transitions per pole, as small changes in curvature at the end of the track were averaged; however despite this, the relative difference in the percentage of lateral transitions per pole observed among conditions tested was clearly maintained (Fig S7C).

SUPPLEMENTAL REFERENCES

Cox, D., Berg, J.S., Cammer, M., Chinegwundoh, J.O., Dale, B.M., Cheney, R.E., and Greenberg, S. (2002). Myosin X is a downstream effector of PI(3)K during phagocytosis. Nat Cell Biol *4*, 469-477.

Kwiatkowski, N., Jelluma, N., Filippakopoulos, P., Soundararajan, M., Manak, M.S., Kwon, M., Choi, H.G., Sim, T., Deveraux, Q.L., Rottmann, S.*, et al.* (2010). Small-molecule kinase inhibitors provide insight into Mps1 cell cycle function. Nat Chem Biol *6*, 359-368.

Rosin, P.L. (2001). Unimodal thresholding. Pattern Recognition, 2083-2096.

Stumpff, J., Wagenbach, M., Franck, A., Asbury, C.L., and Wordeman, L. (2012). Kif18A and chromokinesins confine centromere movements via microtubule growth suppression and spatial control of kinetochore tension. Dev Cell *22*, 1017-1029.

Thoma, C.R., Matov, A., Gutbrodt, K.L., Hoerner, C.R., Smole, Z., Krek, W., and Danuser, G. (2010). Quantitative image analysis identifies pVHL as a key regulator of microtubule dynamic instability. J. Cell Biol. *190*, 991-1003.

Tirnauer, J.S., Canman, J.C., Salmon, E.D., and Mitchison, T.J. (2002). EB1 targets to kinetochores with attached, polymerizing microtubules. Mol. Biol.Cell *13*, 4308-4316.